2008

Aerodynamic mitigation of extreme wind loading on low-rise buildings

Kevin Sehn
Iowa State University

Aerodynamic mitigation of extreme wind loading on low-rise buildings

by

Kevin Sehn

A thesis submitted to the graduate faculty

in partial fulfillment of the requirements for the degree of

MASTER OF SCIENCE

Major: Aerospace Engineering

Program of Study Committee:
Partha Sarkar, Major Professor
Hui Hu
Sivalingam Sritharan

Iowa State University

Ames, Iowa

2008

TABLE OF CONTENTS

LIST OF TABLES

LIST OF FIGURES

ABSTRACT

Hurricanes and other extreme wind events cause immense devastation to our economy every year. Modern buildings should be designed to withstand extreme wind so that it reduces the financial strain on the economy. An experimental study was performed to compare aerodynamic performance of new roof designs. Traditional roof shapes were also included in this study to determine if the new designs had any merit in aerodynamic roof load mitigation. An atmospheric boundary layer wind tunnel was used with the characteristic wind of a suburban boundary terrain. Wind tunnel models were built using a rapid prototyping method. A 1:100 geometric length scale was used for all models. The experiment was performed at one wind speed but repeated for seven building orientations. All six force components of the building were measured using a load cell. The results obtained from measurement of the roof loads showed that the largest reduction was achieved with the leading-edge spoiler, which resulted in 32.3% reduction of roof uplift. A few other methods also demonstrated adequate roof load mitigation. The leading-edge spoiler can be built with the least amount of construction material and it can be easily integrated into an existing or new building. The aerodynamic modification of buildings provides a cost effective solution to reducing the economic impact of hurricanes and other extreme wind phenomena.

CHAPTER 1 INTRODUCTION

1.1 Objective and Motivation

Hurricanes are the costliest wind events in the United States in terms of economic loss: NOAA estimates an average annual U.S. economic loss of $6.3 billion from wind of which hurricanes cause the majority of the damage. The deadliest storm in U.S. history occurred in Galveston, TX in 1900. A category 4 hurricane killed about 6000 people and 700 million dollars in damages. In 1969 the most intense hurricane in U.S. History hit the Gulf Coast. A category 5 hurricane named Camile, killed 256 people (7). In 2005 Hurricane Katrina caused $81.2 billion in damages and killed 1,836 people (8). Statistics show that hurricanes cause economic strain and immense devastation in the United States. As population density on the southeast coastal areas increases, the economic impact of these storms will increase.

The objective of this research is to develop cost effective ways to protect low-rise residential structures from extreme winds caused by hurricanes and other wind phenomena causing strait line winds. A gable roof is one of the most predominant and simplistic roof used for current residential structures. A gable roofed building was studied through wind tunnel investigation to determine any possible improvement that could be developed to make it more wind resistant. Two methods were chosen to achieve this result. The first method was to develop new roof shapes, which could be applied to newly constructed buildings. The second method was to develop economical adaptations to gable roofs in existing buildings. Both the methods were tested in a boundary layer wind tunnel at

Iowa State University. The purpose was to conduct a parametric study to compare the aerodynamic performances of the new roof shapes and adaptations of the existing roofs.

1.2 Thesis Organization

The research presented in this thesis, outlines the development and testing of aerodynamic mitigation models, which have a primary goal of reducing the wind loading around a one-story gable roofed residential building. Chapter 2 provides theoretical background utilized in the development phase. The first section outlines the mechanics of a hurricane and the devastation it causes to our society. The next section provides background in the boundary layer theory of the interaction of a viscous fluid with a solid surface, and flow separation. Boundary layer separation is defined and a separation theory is developed. The last section outlines the research done in the past on bluff body wind mitigation. Chapter 3 provides a detailed description of all models. This chapter provides physical and pictorial descriptions of each model. Chapter 4 describes the experimental setup and procedure used during the experimental phase of the research. Chapter 5 presents the summary of the experimental results. This section also develops the performance index and presents a comparison study utilizing this index. Chapter 6 provides a brief summary of the findings and presents a few conclusions based on these findings. This chapter also presents a set of suggestions and topics for future research. Appendix A contains the graphical results of the aerodynamically modified models. Appendix B contains the graphical results of the aerodynamically adapted models. Appendix C contains the results of the passive pressure equalization models. Appendix D contains the graphical results of all the mitigation models.

CHAPTER 2 BACKGROUND

This research investigates mitigation methods in straight-line wind in an atmospheric boundary layer. Some the natural wind events which cause this type of wind are gusts and hurricanes. Hurricanes cause the most damage therefore a section detailing the growth and decay of a hurricane will be developed in the following section to better understand the mechanics behind this devastating event.

2.1 Hurricane Formation and Dissipation

Hurricanes predominantly form over warm oceans, where a system of thunderstorms exists in regions of low surface pressure. High and low pressure regions tend to form in the tropics because of the difference in atmospheric heating over the land and water. The difference in the flow of air between the ocean surface and land masses is also a source of this pressure variation. A hurricane is a system of thunderstorms with low pressure at its center. The driving force behind hurricanes is condensation. Solar heating causes water vapor to evaporate releasing heat which rises and as this process continues water vapor begins to rise and gets condensed at higher altitude releasing more heat. The low pressure center tends to draw air to the center, but the Coriolis effect (caused by the rotation of earth) causes a counterclockwise rotation in the Northern Hemisphere about the low pressure region. As the air rotates towards the center it is forced upwards turning into mechanical energy. This energy increases the wind speeds, which in turn increase the surface evaporation and the vapor condensation fueling the hurricane. The

released energy causes updrafts which increase the height of the storm accelerating the condensing process. As the hurricane develops, it becomes more difficult for air to reach the center. The centrifugal force of the stronger winds at the center tends to force the air outward. This motion results in the formation of rain bands (Figure 2.1).

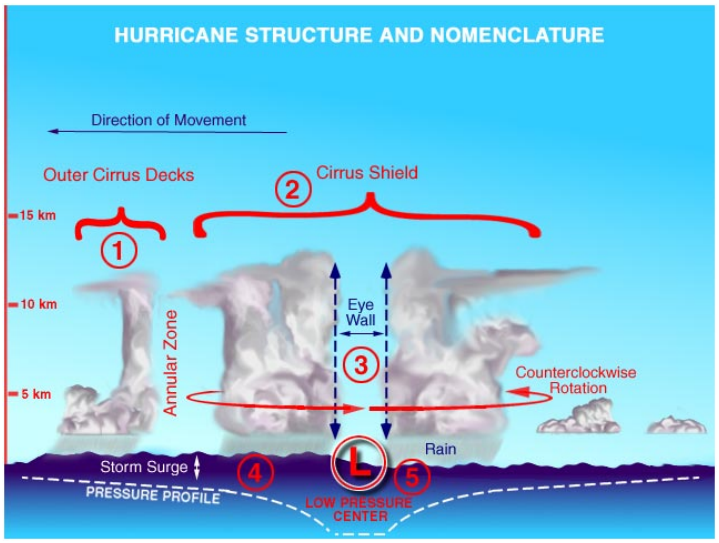

Figure 2.1 Structure of a tropical hurricane (9)

As the tropical storm becomes fully developed and reaches the lowest hurricane category, the air can no longer reach the center. A region of calm weather forms at the center called the eye. The eye wall surrounds the eye of the hurricane, which is a region closest to the center and therefore has the largest spiraling inward air with the strongest winds. The hurricane has enough energy to become self sustaining. A hurricane will eventually decay as a result of four causes; dry air, mountainous land regions, cool ocean surface water, and dry land. Dry air coming off land can slow down the condensation process. Mountainous land regions can affect the inflow into the center of the hurricane, disrupting the flow and weakening the hurricane. As the hurricane makes landfall, it no longer has access to sufficient warm water over the dry land and therefore the winds in the eye wall decrease and the pressure increases at the center of the low pressure region, diminishing the strength of the hurricane (17).

Cat	Wind Speeds (mph) (1 min. avg.) (mph)	Central Pressure (mb)	Storm Surge (above normal) (ft)	Description
1	74 - 95	> 980	4 - 5	No damage to building structures
2	96 - 110	965 - 979	6 - 8	Some roof, door and window damage of buildings
3	111 - 130	945-964	9 - 12	Some structural damage to residences and utility buildings
4	131 - 155	920 - 944	13 - 18	Some complete roof structure failures
5	> 155	< 920	> 18	Some complete building failures

Table 2.1 Saffir-Simpson hurricane scale (19)

A hurricane is rated by the Saffir-Simpson scale (Table 2.1), which is a category rating to represent the intensity of a hurricane. The rating is used to predict potential property damage and flooding that may occur from a hurricane landfall. The reason hurricanes are so damaging is because of storm surge. Storm surge is the ocean water a hurricane pushes up on land as it makes landfall (17). A category 4 hurricane can actually have a higher storm surge than a category 5 hurricane, therefore causing more property damage. The Gulf coast is particularly affected by the storm surge because of the continental shelf which causes waters to rise even higher. Hurricane season typically runs from June to November in the United States with the peak occurring in August and September.

2.2 Boundary Layer Theory and Flow Separation

The topic of this research is three-dimensional, unsteady, turbulent flow of a stream of incompressible viscous fluid past a bluff body. A critical step to develop the mitigation methods was to understand boundary layer theory and utilize this information to control

boundary layer separation. This section provides the theory used during the development of the mitigation methods.

The analytical solution to the viscous equations of motion, conservation of mass, momentum, and energy, are extremely complicated. The equations of motion were derived for viscous flow by Navier (1827) and Stokes (1845),(Eq.2.1, Eq.2.2, Eq.2.3).

$$\rho(\frac{\partial u}{\partial t} + u\frac{\partial u}{\partial x} + v\frac{\partial u}{\partial y} + w\frac{\partial u}{\partial z}) = -\frac{\partial p}{\partial x} + \mu(\frac{\partial^2 u}{\partial x^2} + \frac{\partial^2 u}{\partial y^2} + \frac{\partial^2 u}{\partial z^2}) + \rho g_x \tag{2.1}$$

$$\rho(\frac{\partial v}{\partial t} + u\frac{\partial v}{\partial x} + v\frac{\partial v}{\partial y} + w\frac{\partial v}{\partial z}) = -\frac{\partial p}{\partial y} + \mu(\frac{\partial^2 v}{\partial x^2} + \frac{\partial^2 v}{\partial y^2} + \frac{\partial^2 v}{\partial z^2}) + \rho g_y \tag{2.2}$$

$$\rho(\frac{\partial w}{\partial t} + u\frac{\partial w}{\partial x} + v\frac{\partial w}{\partial y} + w\frac{\partial w}{\partial z}) = -\frac{\partial p}{\partial z} + \mu(\frac{\partial^2 w}{\partial x^2} + \frac{\partial^2 w}{\partial y^2} + \frac{\partial^2 w}{\partial z^2}) + \rho g_z \tag{2.3}$$

The Navier-Stokes equations are non-linear partial differential equations. Exact solutions are only obtainable for specific cases, such as an incompressible fluid with unidirectional or circular steady streamlines. The physical characteristics of this type of flow allow the Navier-Stokes equations to be simplified into linear equations. Some examples of this type of flow are plane couette flow and plane poiseuille flow through two parallel plates (Figure 2.2).

As a viscous fluid flows past a body, two types of drag are possible: form drag due to separation of the flow from the body, and skin friction caused by the contact of the fluid with the body. A bluff body is primarily governed by form drag. Form drag is the integration of the pressure forces over the body surface along the direction of the flow. Skin friction acts tangentially to the surface where the flow remains attached and therefore is neglected because the flow over the majority of the surface is typically separated (20).

The difference between inviscid and viscous fluids is the boundary conditions: the no-slip condition, and the dominance of the viscous boundary layer in the flow. The

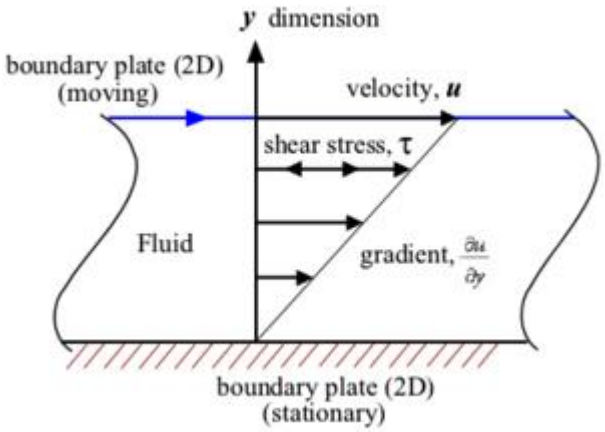

Figure 2.2 Plane couette flow between two parallel plates

no-slip condition states that the velocity of the fluid at the wall is zero. For an inviscid solution the velocity component normal to the surface is zero, but for a viscous fluid the total velocity is zero (11).

A boundary layer is a region next to the body surface boundary, which viscous effects govern the fluid. If the boundary layer remains thin and attached to the body, the flow outside the thin boundary layer will closely reflect the inviscid solution, and the solution will follow potential theory. This type of flow has very little form drag and skin friction is the predominant component of drag. As viscous drag increases, it dissipates energy from the flow. Eventually there will be an insufficient amount of energy to traverse a blunt body. If separation occurs, a wake is created, therefore changing the pressure distribution on the body from the potential solution and increasing the form drag. Typically for a bluff body separation occurs on the roof, side walls, and leeward wall. Boundary layer theory states that separation occurs when the convection terms in the x-momentum equation at the body surface (Eq. 2.4) approach zero. At this point the stream-wise pressure gradient is positive or adverse, ($\frac{\partial p}{\partial x} > 0$). From Eq. 2.4, the pressure gradient ($\frac{\partial p}{\partial x}$) and ($\frac{\partial^2 u}{\partial y^2}$) must have the same sign at the surface boundary (11).

$$\frac{1}{\mu}(\frac{\partial p}{\partial x}) = (\frac{\partial^2 u}{\partial y^2})_{y=0} \tag{2.4}$$

A pressure gradient is positive when the pressure force is in the direction to decelerate the flow. A positive pressure gradient exists when the static pressure increases in the direction of the flow. The increase in pressure causes an increase in potential energy of the fluid and a decrease in kinetic energy, retarding the flow. At the separation point, the slope of the velocity component normal to the surface ($\frac{\partial u}{\partial y}$) is zero at the wall and at the boundary layer thickness. Downstream of this point, $\frac{\partial u}{\partial y} < 0$, at the wall, and flow reversal can be seen close to the surface. In this region, flow is considered separated and the body surface will encounter negative pressures or suctions. The velocity inside the boundary layer increases from zero at the surface, as stated in the no-slip condition, to a positive value outside the boundary layer. Since $\frac{\partial u}{\partial y} < 0$ at the wall and $\frac{\partial u}{\partial y} = 0$ at the boundary layer thickness $\frac{\partial u}{\partial y}$ will increase along the y-axis in the boundary layer. Therefore, $\frac{\partial u}{\partial y}$ must attain a maximum at some point before it begins to decrease again. At this point $\frac{\partial^2 u}{\partial y^2} = 0$, the velocity profile contains an inflection point (Figure 2.3).

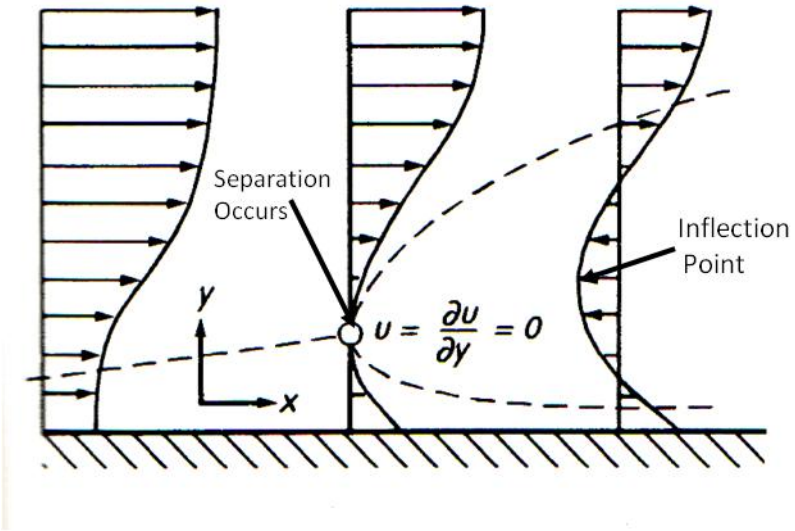

Figure 2.3 Boundary layer separation over a solid surface

A inflection point is a location on the curve at which the curvature changes sign. Upstream of the separation point, $\frac{\partial u}{\partial y} > 0$ at the wall, and $\frac{\partial p}{\partial x} < 0$ which will accelerate the fluid along the surface, thinning out the boundary layer. At this point, outside the separation bubble $\frac{\partial u}{\partial y}$ is decreasing as we move along the y-axis until it approaches zero and no inflection point will exist (11). To make a gable roofed building withstand higher winds, separation needs to be delayed or minimized to reduce form drag. Boundary layer control methods can be used to accomplish this task and create more wind resistant homes.

2.3 Past Aerodynamic Roof Mitigation Research

Past and current research in bluff body wind mitigation has focused primarily on reducing the surface pressure on flat roofed buildings or rectangular prisms. Wu and Sarkar (2000) pioneered the research in a specific parapet (Figure 2.4) called a Conical Vortex Disrupter.

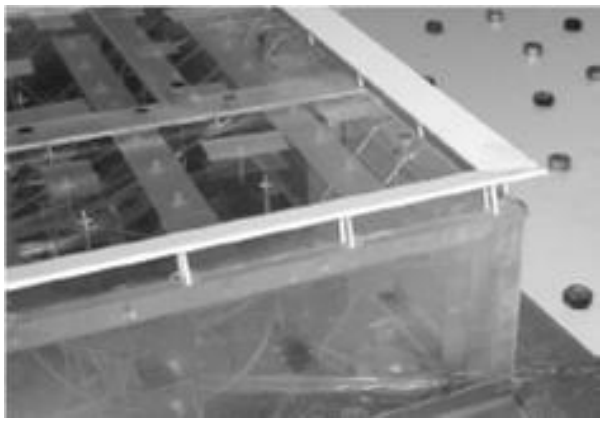

Figure 2.4 Parapet roof attachment along leading-edge of building

They showed through a full-scale test that the device significantly reduced both local and area-averaged wind loads near the roof corners on a flat roofed building. The research done by Kopp, Mans, and Surry (2005) also studied the wind effects of parapets

on low-rise flat roofed buildings. They performed a parametric study of different types of parapets and found that perimetric spoilers and porous parapets effectively reduced the roof loads as much as 50%. They also showed that isolated parapets (only on one wall) tend to increase the corner delta vortices causing more suction on the roof. The research done by Pindado and Meseguer (2003) also studied the effects of different parapets on reducing roof pressures on low-rise flat roofed building. This research validated the conclusions of Kopp, Mans, and Surry (2005). Pindado and Meseguer research demonstrated that spoiler parapets are only effective at relatively low parapet height, as compared to the building height. Cheng and Melbourne (1988) researched the effects of a porous roof on reducing the roof pressures. The study showed significant reduction in the peak and mean roof pressures. The reduction increased as porosity increased and as the internal volume decreased. The study produced a maximum decrease in roof pressure of 20% near the leading-edge, and 30% in the downstream region. The study by Munshi, Modi, and Yokomizo (1999) demonstrated the effectiveness of a rotating circular cylinder as a form of boundary layer control. They looked at drag reduction on a bluff body, a rectangular prism. The results showed peak reductions between 60% and 85% in drag and significant suppression of vortex shedding.

Mitigation research has been done on other roof shapes such as a hip roof by Meecham (1992) and curved roofs by Meseguer et al. (2005). Meecham researched the benefits of hip roof construction. Meecham's results demonstrated peak roof pressure reductions up to 50% (compared to a gable roof) and showed that a hip roof can without failure handle winds speeds 30% larger than a comparable gable roof. Pindado and Meseguer used their previous results in corroboration with Franchini and Sanz-Andres (2005). A leading-edge perimetric spoiler parapet was used to reduce the conical vortices on a curved roof. The results showed a reduction in the corner vortices and a significantly lower peak and mean pressure on the curved roof. A study done by Modi, Fernando, and Yokomizo (1991) applied the concept of a rotating cylinder to a semi-truck and

trailer. The results showed drag reduction up to 23%, and found surface roughness of the rotating cylinder increases the reduction. They also found the effectiveness of the concept is reduced if the cylinder is located in the wake.

All past research has focused on pressure and flow measurement. This type of research is vital to understanding the mechanics of the flow, but little work has been done to determine how this flow translates into forces around the body. For this reason this research will focus on load measurement. Specifically, experimental investigation of how much load reduction is possible on a one-story gable roof residential building.

CHAPTER 3 MITIGATION BUILDING MODELS

3.1 Base Building Models

3.1.1 Gable Roof Model

The gable roof is one of the most commonly built roofs in residential construction. This model will be used as a base model for comparison. This model was designed to mimic the modern residential building architecture. A rapid prototyping method was used to create all models. This method uses solid works to model the buildings and a rapid prototyping machine to construct the 3D model out of ABS plastic. A solid works image of the finished gable roofed model can be seen in Figure 3.1.

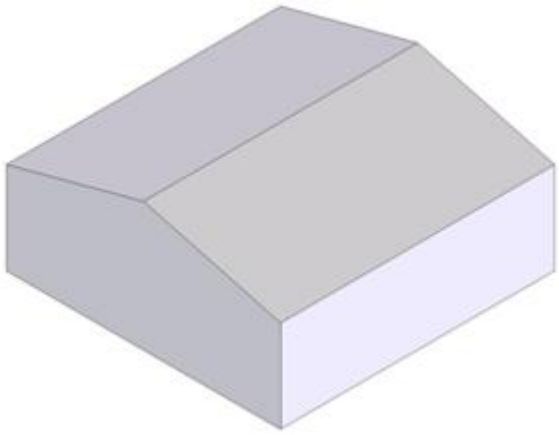

Figure 3.1 Solidworks drawing of the gable roof base model

Loads were measured on a 1:100 scaled model of a one-story gable roof building. The

model had a 3.6 in. by 3.6 in. plan length and width, respectively. The building ridge height was 1.6375 in. and the eave height was 1.2 in. The pitch of the roof was $\frac{3}{12}$ or 13.66°. This roof slope was chosen because past research (1) has shown the worst case of roof uplift occurs at a shallow roof slope. The full-scale building would have a 30 ft. by 30 ft. plan length and width, respectively, and eave height of 10 ft. The length scale limited the amount of details in the models. The finer details of the full-scale building were ignored in the model because of the simplification used in the modeling. Building roof overhang, roof shingles, and exterior siding were all ignored in the model. The roof of the model was sanded smooth and the leading-edge of the roof was flushed with the building walls as can be seen in Figure 3.1.

3.1.2 Hip Roof Model

The hip roof is another roof shape used in residential building construction. Hip roof design performs better than traditional gable roofs. As stated in Section 2.3, hip roofs reduce the magnitude of the mean negative pressures on the roof. The total uplift between the two roof shapes were not significantly different, but the geometry of the hip roof reduces the mean negative peak pressures areas on the leading-edge of the roof and increases the amplitude of the mean negative pressures further downstream on the trailing-edge of the roof. Redistribution of pressure has little effect on the total uplift but reduces the mean peak pressures. The mean peak pressure reduction allows the hip roof to remain intact, whereas a similarly constructed gable roof would have failed because of high negative pressures near the leading-edge as stated by Meecham (1992). The basic hip roof model will be used here to compare the effectiveness of the new roof designs. New roof designs whose aerodynamic performance is worse than the hip roof are not very effective solutions because the hip roof is used in modern construction, and currently the most cost effective. The hip roofed base model can be seen in Figure 3.2, which has the same plan length, plan width, ridge height, and eave height as the gable

roofed base model. The hip roof has a $\frac{3}{12}$ slope perpendicular to the ridge and a $\frac{6}{12}$ slope parallel to the ridge which are 13.66°, and 27.32° angles, respectively. The projected area, Ay, used in one of the non-dimensional force coefficients for this shape is different from the gable roof base model, as defined in Figure 4.11, all other areas remained the same.

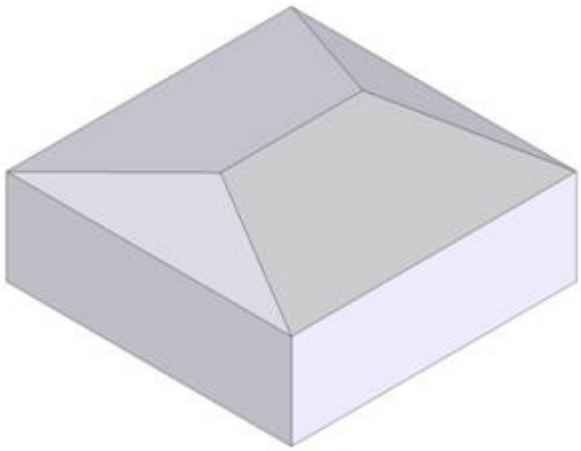

Figure 3.2 Solidworks drawing of the hip roof model

3.2 Aerodynamically Modified Building Models

The next set of models were tested to check their performance for wind-induced load mitigation through aerodynamically modified roof shapes. The primary objective of these modified roof designs is to provide adequate load mitigation while maintaining a commercially marketable roofs. These roofs must be specifically designed to accommodate a truss structure underneath. An aerodynamically modified roof shape would provide a passive mitigation method which could be incorporated into future residential buildings. These models are described below. The current study on mitigation is done by modifying the gable roof base model. The same concept could be applied to a hip

roof building.

3.2.1 Variable Sloped Roof Model

As the name implies, a variable sloped roof is an aerodynamically modified roof shape with discretely variable roof slope. The gable roof was split into three sections, as seen in Figure 3.3. A course division was chosen because it would allow easier fabrication of the truss that supports it when implemented in construction.

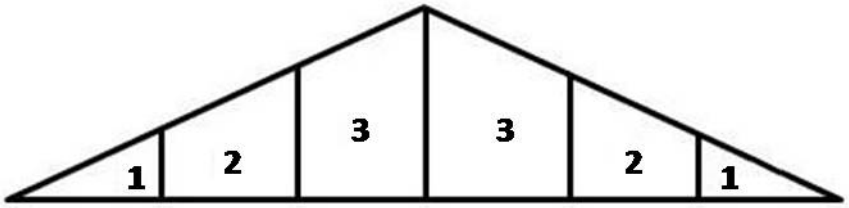

Figure 3.3 Gable roof truss section division

The sections were modified in two ways: one model had increasing roof slope, and the other had a decreasing roof slope. The variable increasing sloped roof (VISR) can be seen in Figure 3.4, which starts with an 8° slope and ends with a 30° slope while the middle section has the smallest slope of 3°.

The variable decreasing sloped roof (VDSR) can be seen in Figure 3.5. Section one has a 26° slope, section two has a 10° slope, and section three has a 4° slope. The aerodynamic concept behind the VISR shape is that as the roof surface is lowered, it creates a valley so that separated flow near the leading-edge of the roof is lowered. This brings the shear layer closer to the roof surface, which reduces the suction on the roof and the associated form drag. The assumed aerodynamic concept behind the VDSR shape is that the roof surface tries to take the form of the contour of the streamlines of the flow. This could allow the flow to remain attached on the windward side although the flow would still separate on the leeward side of the roof. This shape should also reduce the separation on the leeward side by bringing the roof surface closer to the

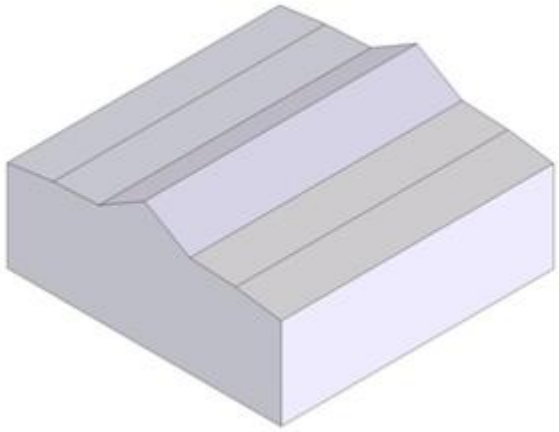

Figure 3.4 Solidworks drawing of the variable increasing sloped roof model

shear layer. This allows the flow to remain attached longer because the curvature is more streamlined which delays the onset of an adverse pressure gradient.

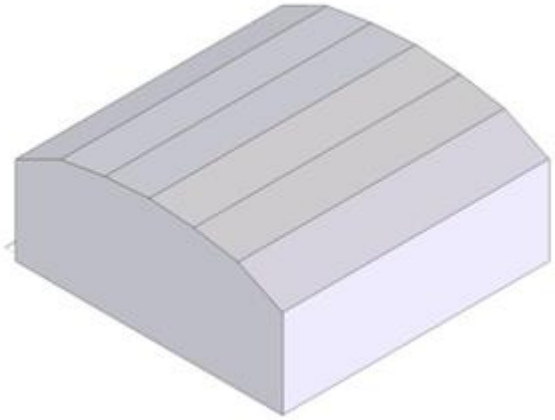

Figure 3.5 Solidworks drawing of the variable decreasing sloped roof model

Both the VISR and the VDSR models have the same plan length, plan width, ridge height, and eave height as the gable roof base model. These shapes are symmetric about the ridge. The projected area, Ax, used in one of the non-dimensional force coefficients for these shapes is different from the gable base model, as defined in Figure 4.11, all

other areas remaining the same.

3.2.2 Curved Corner Model

In bluff body aerodynamics, the flow always separates around a 90° corner or a sharp edged corner. A building with curved corners allows for delayed separation to occur further downstream reducing the separation bubble and the form drag. This concept of streamlining the wall corners of the building was studied as a passive means to reduce the drag either to compensate for increased drag (if any) from modified roof shapes or reduce the drag of the gable roofed base model. The latter was studied here. This shape would have little or no effect on the uplift. A solid works drawing of the streamlined rapid prototyped model can be seen in Figure 3.6.

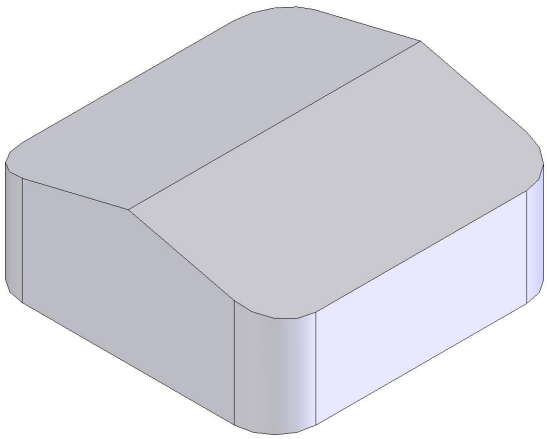

Figure 3.6 Solidworks drawing of the streamlined wall model

The curved corner model has the same plan length, plan width, ridge height, eave height, and roof slope as the gable roof base model. The projected areas used to define the non-dimensional force coefficients are the same as the gable base model as defined in Figure 4.11 except the projected area in the z-direction (Az) which now includes the curved corners.

3.3 Aerodynamically Adapted Building Models

The next set of models provide aerodynamic mitigation by adding an attachment to the existing gable roof structure. The primary objective of these aerodynamic attachments is to provide adequate wind load mitigation that can be economically implemented in existing residential buildings while maintaining an aesthetically pleasing architecture. Most of the concepts in this section can be classified as passive methods although a few can be classified as active methods of mitigation. Active methods require use of energy and in today's market energy efficiency is important. However, aerodynamic mitigation will be required only when extreme wind occurs so the energy requirement is minimal. Since passive methods are simpler and require no energy to control the performance, these are preferable to the active methods and will be the focus of this study. All models in this section use the rapid prototyped gable roof base model that is modified with different attachments to create the mitigation model. All dimensions and projected areas used in the calculation of the non-dimensional force coefficients for these cases are the same as the gable roof base model. All models were designed for force measurement and fitted with an internal structure to accommodate the force transducer.

3.3.1 Edge Spoiler Models

The edge spoiler attachment is a method to reduce the high suction caused by the conical delta vortices. The edge spoiler is placed along the roof edge and along the ridgeline as seen in Figure 3.7. The edge spoiler provides mitigation by separating the flow into two parts; one underneath the spoiler, and one above that forms the vortex. A high pressure region forms in front of the spoiler and a low pressure region forms behind it. This pressure gradient injects a stream of flow underneath the spoiler into the roof vortex in the opposite direction of the vortex rotation, alleviating the vortex strength, and thereby reducing the roof loads. The method will require a minimal

amount of material and should also be relatively easy to incorporate into an already existing structure. The architectural design of the building is conserved because the spoiler is effective at relatively low heights. This concept has been successfully tested on a flat roofed building by Wu and Sarkar (2000).

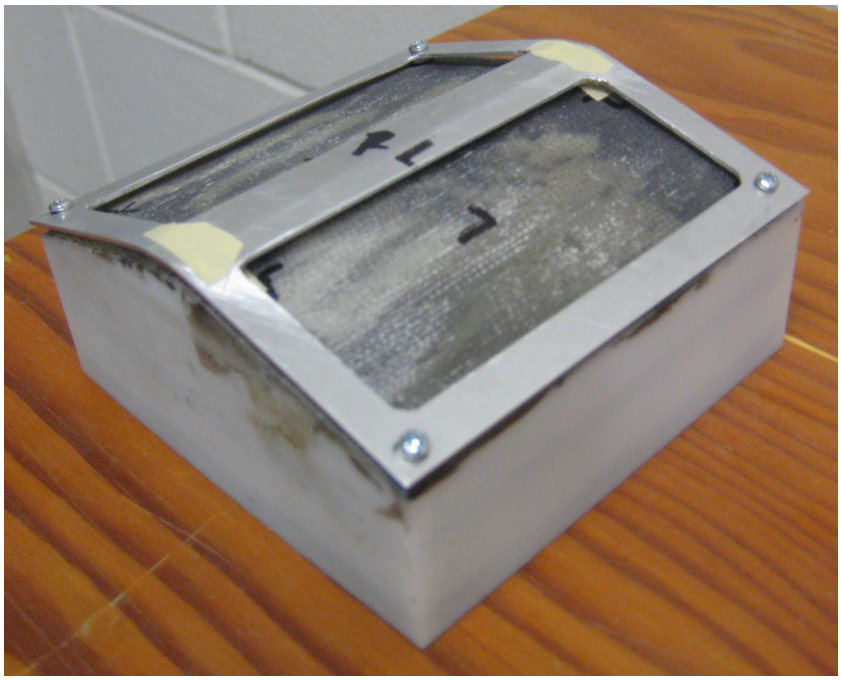

Figure 3.7 Flush edge spoiler model

The edge spoiler is made out of a flat strip of aluminum that is fixed slightly above the roof of the gable base model as shown in Figure 3.7. The spoiler has a thickness of 0.042 in., a width of 0.25 in., and a spacing above the roof surface of 0.042 in. Two types of attachments were tested; one that was flush with the side of the building, and the other had a 0.125 in. overhang beyond the side wall. The spacing underneath the spoiler remained the same for both attachments. In Figure 3.7, the attachments were installed along the outside edge of the roof and along the ridge. Each of the two attachments was made as a single piece which was mounted to the roof at the four corners.

3.3.2 Porous Canopy Roof Models

The porous canopy roof attachment is a method which uses a porous cover to conceal the existing roof (Figure 3.8).

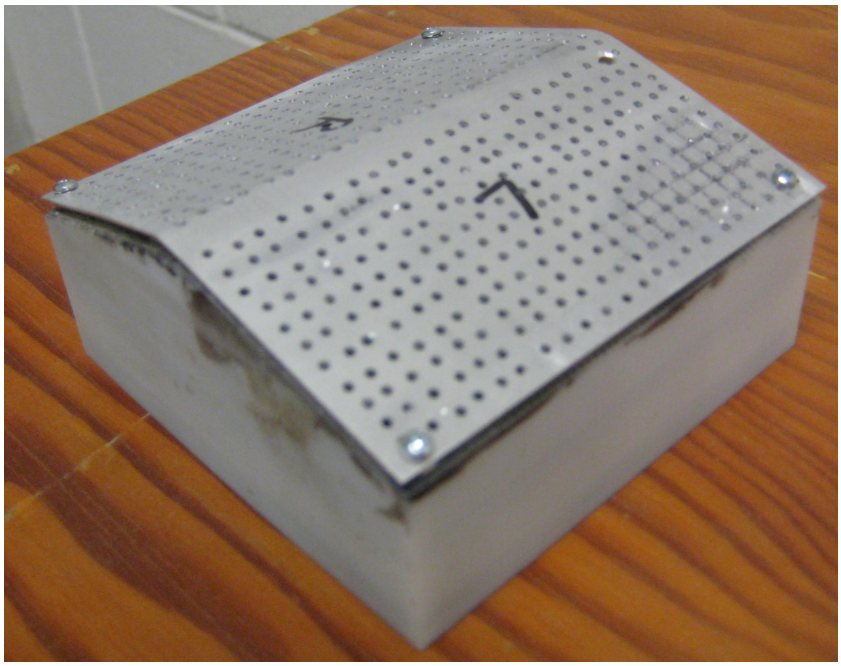

Figure 3.8 Porous canopy roof model (10% porosity)

This method was expected to reduce the mean and peak pressures on the roof. The practicality of this method is that the canopy provides a false cover, while maintaining the waterproof roof structure underneath it. Several issues would exist if this method is implemented into current construction because snow or environmental debris such as, dirt, insects, plants, and twigs could possibly block the pores of the canopy. Some method would be needed to maintain the porosity of the canopy if this method was to have practical use. The porous canopy roof attachment provides mean and peak roof pressure reduction by allowing the air to flow through the pores on the false roof surface into the internal space between the canopy and waterproof roof. This will create a thin layer of air in between the two surfaces creating a positive mean pressure under the top surface that partially balances the fluctuating negative peak pressures on the

canopy surface. The porous canopy is made of a 0.042 in. thick aluminum plate. Two types of canopies were tested; one was 1% porous, and the other was 10% porous. The 10% porous canopy can be seen in Figure 3.8. The 1% canopy top had 64 (0.0625 in. diameter) holes, and the 10% canopy top had 484 (0.0625 in. diameter) holes evenly spaced across the surface. The attachment was spaced 0.042 in. above the roof surface and mounted at the four corners of the roof. This spacing is similar to the edge spoiler.

3.3.3 Passive Pressure Equalization Models

The passive roof pressure equalization method uses pressure tubing to connect openings on the windward side to openings on the leeward side of the roof. This model can be seen in Figure 3.9.

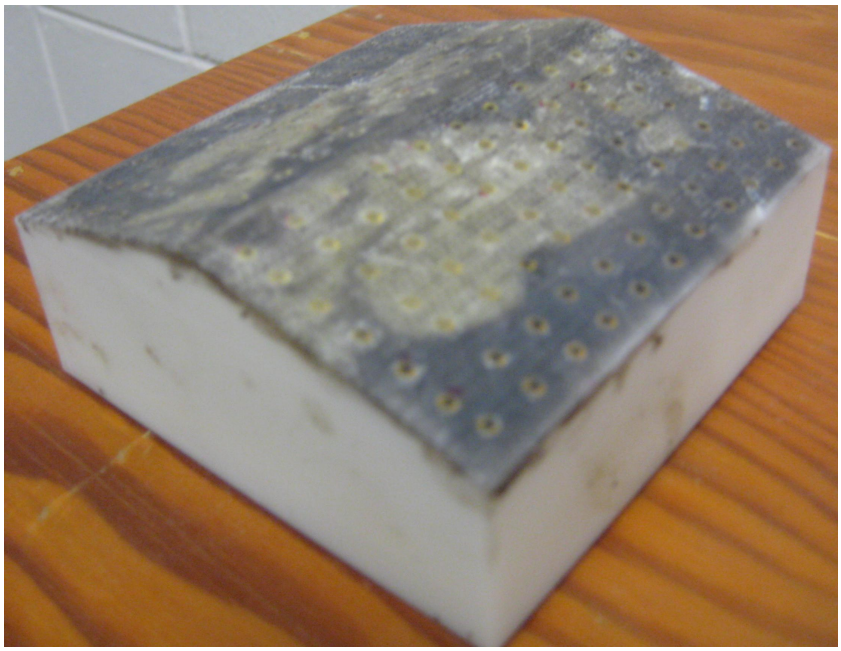

Figure 3.9 Passive roof pressure equalization model

This passive method can potentially reduce the large suction on the leeward side of the roof by equalizing with the smaller suction on the windward side. This method, like the porous canopy roof, also has practical issues associated with construction and

implementation. For practical use, a method needs to be developed to prevent blockage of the roof openings from environmental debris. A method also needs to be developed to prevent moisture build-up inside the tubing. The method studied in this research is a passive method, but an active method using a powered vacuum reservoir could reduce the wind loading on the windward side, leeward side, and the side walls. This active method would prevent or reduce separation by removing flow that has low momentum. Another issue which limits the usefulness of this method is the complexity of implementation of this technique. Pressure tubes have to be run through the internal volume of the roof. This would be a tedious process which would require time and money. A passive method to reduce the drag on the building was also developed that utilizes the same principles. Pressure tubes were used to connect openings on the windward wall to the leeward wall. This model can be seen in Figure 3.10.

Figure 3.10 Passive wall pressure equalization model

The wind tunnel models used to test the passive pressure equalization method have the same dimensions as the gable base model. For the passive roof pressure equalization model, 77 holes were drilled into the windward side of the plastic roof surface and connected to 77 holes drilled into the leeward side of the plastic roof surface. The holes were connected with pressure tubing with a 0.0625 in. inside diameter. The holes were

evenly spaced across the roof surface and the holes on the windward side were connected to a similar location on the leeward side. The passive wall pressure equalization model used 15 holes that were connected between the walls perpendicular to the ridge and 12 holes that were connected between the walls parallel to the ridge, (Figure 3.10). The walls were connected using the same pressure tubing as with the previous model. The holes were evenly spaced across the walls and each hole on the wall was connected to a hole in a similar location on the opposite wall.

3.3.4 Momentum Injection Model

The momentum injection method to control boundary layer separation, consists of a rotating cylinder mounted along the ridge of the model as seen in Figure 3.11. The rotating cylinder delays or eliminates boundary layer separation in two ways; by reducing the relative motion, and by injecting momentum into the boundary layer. The difference in the motion of the flow and the body surface creates the boundary layer. A moving surface, which moves in the same direction as the flow, helps reduce the relative velocity between the body surface and the free stream flow. This reduction in the relative velocity helps control the boundary layer separation. The cylinder also injects momentum into the low momentum boundary layer by rotating the fluid around the cylinder into the separated flow on the leeward side of the roof. The effects of these two events are delay in separation, acceleration of the flow immediately outside the boundary layer, and reduction of the wake. This method can be controlled by two means; passive and active. Although wind tunnel testing was not completed for either of these methods, the momentum injection model was develop and prepared for wind tunnel testing in future experiments. The active control will use a small DC motor (Figure 3.12) mounted inside the model that will drive the cylinder rotation. The Passive method will use two small wind turbines mounted axially to the cylinder, located on each side of the building. The model consists of a 0.625 in. diameter circular cylinder with a 3.3125 in. length (Figure

3.11). The cylinder will spin on high speed ball bearings (Figure 3.11) mounted at the ends of the ridge. The cylinder will be rotated using a drive chain connecting the cylinder and the motor. The DC motor has a nominal voltage range of 1.5 volts to 3.1 volts, and will be controlled with a DC power supply (Figure 3.12). The model will allow the height of the cylinder to vary as well as the cylinder rotational speed. Initial testing needs to be performed to determine which configuration provides the most aerodynamic mitigation. Due to the complexity of this model, the wind tunnel testing was not performed in this study. The model is fully developed and ready to begin wind tunnel testing.

Figure 3.11 Rotating cylinder momentum injection model

Figure 3.12 DC power supply and electric motor assembly

CHAPTER 4 EXPERIMENTAL PROCEDURE

4.1 Wind Tunnel and Boundary Layer Setup

All the wind tunnel tests were performed in the AABL wind and gust tunnel that is located in the ISU WiST Lab at Iowa State University. The AABL wind and gust tunnel is a closed circuit wind tunnel with a capacity to generate wind speeds exceeding 90 mph in the test section that is 8 ft. wide and 7.5 ft. high. There is a rotating turntable where the models in the test section can be mounted to test for different wind directions. A suburban boundary layer was used for this study. The roughness elements used to generate the suburban boundary layer can be seen in Figure 4.1. The elements for generating the suburban boundary layer consisted of spires, blocks, and chains. Spires are triangle-shaped protrusions in the flow which cause more perturbation at the bottom than the top. There were 4 spires located at 50 ft. upstream of the model center. The spires are 0.75 ft. wide at the bottom and 4.5 ft. high, and the tips of each spire are spaced 1.67 ft. apart from the wall and each other. The blocks are 0.208 ft. tall and there is a 1.125 ft. space between blocks in all directions. The blocks were arranged in 30 rows starting at 42.3 ft. from the center of the model and ending at 4.8 ft. from the center of the model. The odd rows of blocks started at 0.208 ft. from the side of the tunnel. The even rows of blocks started at 0.833 ft. from the side of the tunnel. The chains were used to maintain the turbulence in the flow in the region between the model and the last row of blocks. The chain was 0.5 in. thick, and was laid in rows starting at 3.5 ft. from the center of the model and ending at 0.79 ft. from the center of the model.

The chain was arranged in three rows spaced 1.375 ft. apart.

Figure 4.1 AABL wind and gust tunnel

The velocity profile and the turbulence intensity profile for the boundary layer were measured using a hot-wire anemometer in (10)(Figures 4.2 and 4.3). The profiles were verified in this study with a Cobra probe as described in the next section. The wind speed increases in an atmospheric boundary layer with height above the ground. The streamwise wind profile follows a power law (Equation 4.1) as given below.

$$\frac{U(z_1)}{U(z_2)} = (\frac{z_1}{z_2})^{\alpha} \tag{4.1}$$

The power law exponent (α) for a suburban boundary layer can range from approximately 0.2 to 0.3. The power law exponent calculated for the suburban boundary layer used in all the experiments in this study was 0.22. The roughness length (z_o) of the suburban boundary layer used in the experiment was 0.00215 ft. above the ground plane. The turbulence intensity was 23% at 33 ft. (full-scale) equivalent height.

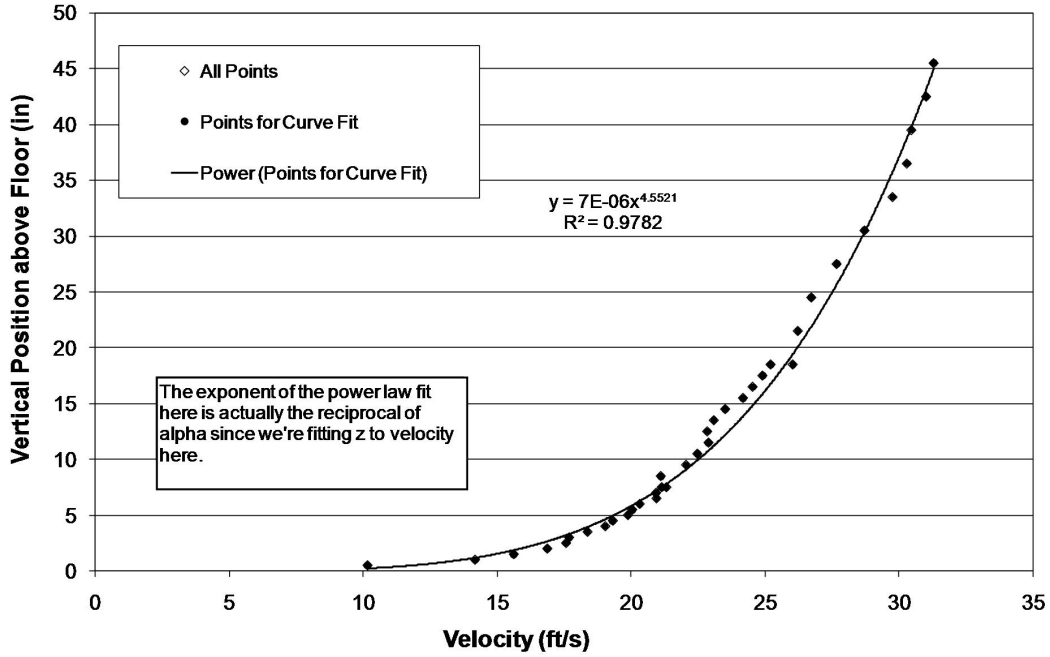

Figure 4.2 Streamwise velocity profile as reported in (10)

4.2 Experimental Instrumentation Setup

The boundary layer profiles were taken using a multi-hole pressure probe called Cobra probe (Figure 4.4). The Cobra probe provides three component velocity (magnitude and direction) and local static pressure measurements in real time. The Cobra probe has a frequency response of up to 2000 Hz which makes the probe specifically suited to measure turbulent flow. The probe measures the flow field within a range of ±45 degrees from its axis. The Cobra probe has an accuracy of $\pm 1.6\frac{ft}{s}$ ($\pm 0.5\frac{m}{s}$) and ±1 degree for pitch and yaw angles, this accuracy is effective up to 30% turbulence intensity. For turbulent flow with turbulence intensity greater than 30%, the probe is still relatively accurate. The computer setup (Figure 4.4) inputs the raw voltage from the probe to a data acquisition interface unit (Figure 4.4), which is connected to the computer using a data acquisition card. TFI Device Control software is used to control the probe and analyze the raw output. The voltage output from the probe is converted to velocity data by the TFI

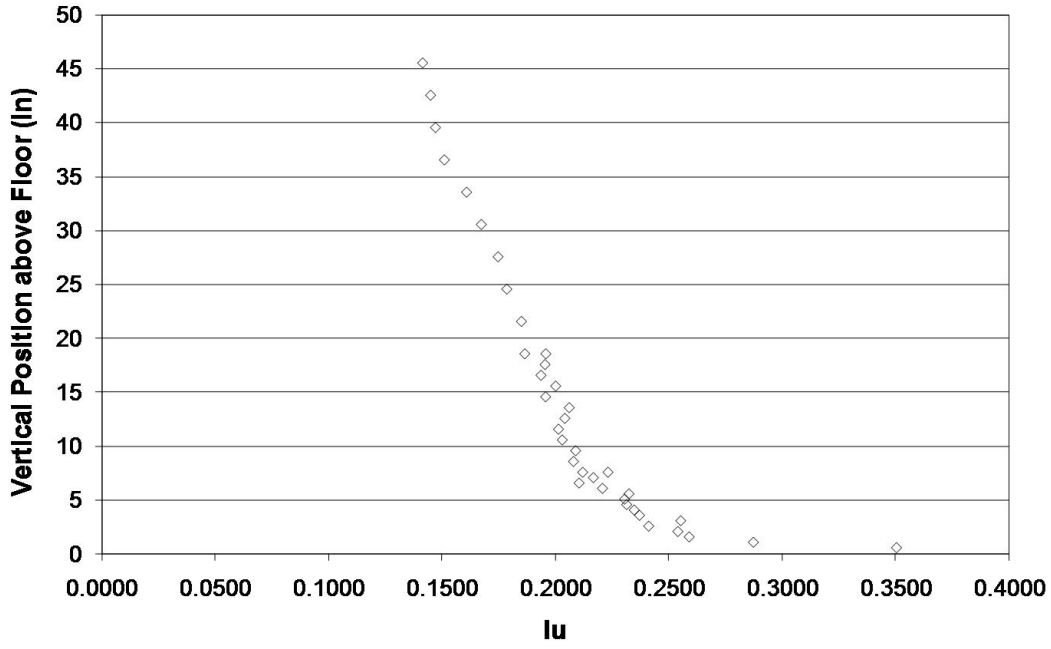

Figure 4.3 Streamwise turbulence intensity profile as reported in (10)

Device Control software. The device was calibrated in the factory, therefore no initial calibration was required.

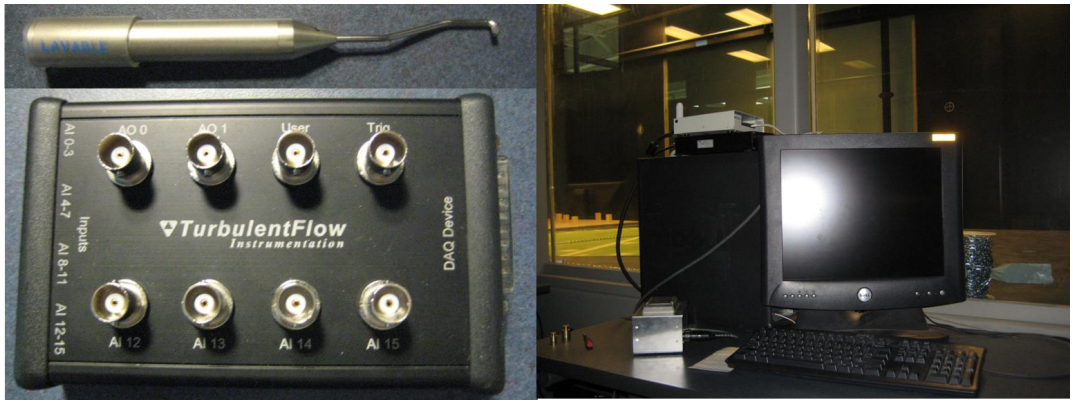

Figure 4.4 Data acquisition system setup

The velocity during the experiment was checked periodically to maintain an accurate comparison. The velocity profiles and turbulence intensity profiles were taken using the cobra probe. The velocity measurements at a wind tunnel motor frequency setting of

15 Hz were taken with a 500 Hz sampling rate over a period of 60 seconds. The Cobra-probe velocity profile and turbulence intensity profile can be seen in Figures 4.5 and 4.6. These profiles agree well with the profiles in Figures 4.2 and 4.3.

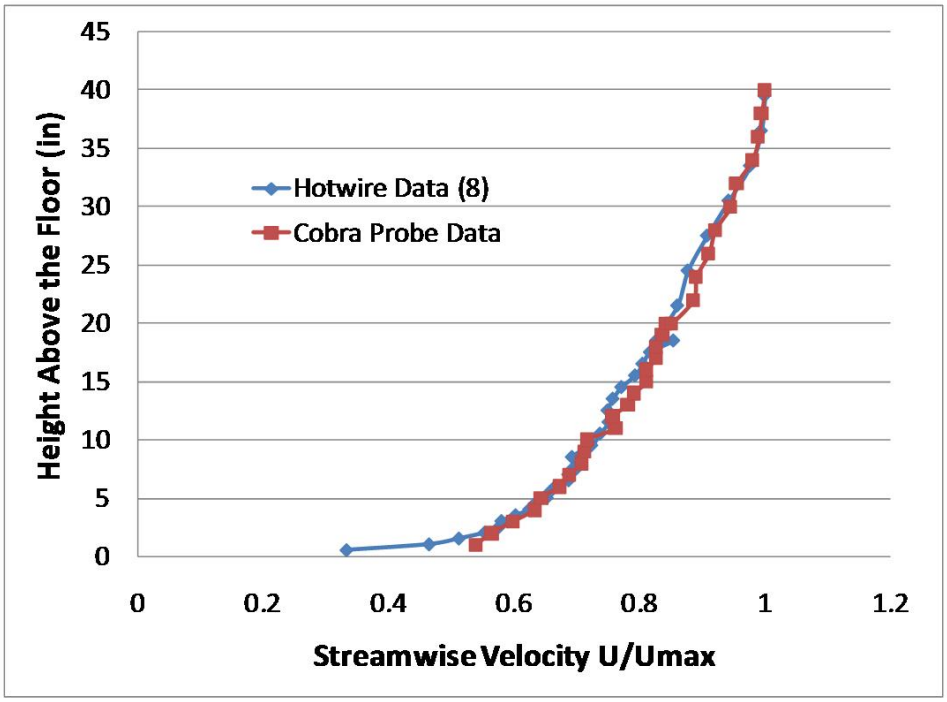

Figure 4.5 Streamwise velocity profiles

The load measurements were taken using a multi-axis force sensor system called JR3 (Figure 4.7). The JR3 can measure three components of force and moment along the three orthogonal axes in real time. The data acquisition system setup (Figure 4.8) consists of a computer, power supply, and a data junction box. The system takes the voltage output from the JR3 and sends it to the data acquisition software, a Labview program (national instruments), which converts the raw voltage to force and moment. The JR3 was calibrated in the factory, therefore no initial calibration was required.

The JR3 was mounted on the bottom of the turntable while an aluminum rod fixed to the building model at one end and threaded through the center of JR3 at the other end, transfers the forces and moments from the model to the JR3 (Figure 4.7). A small

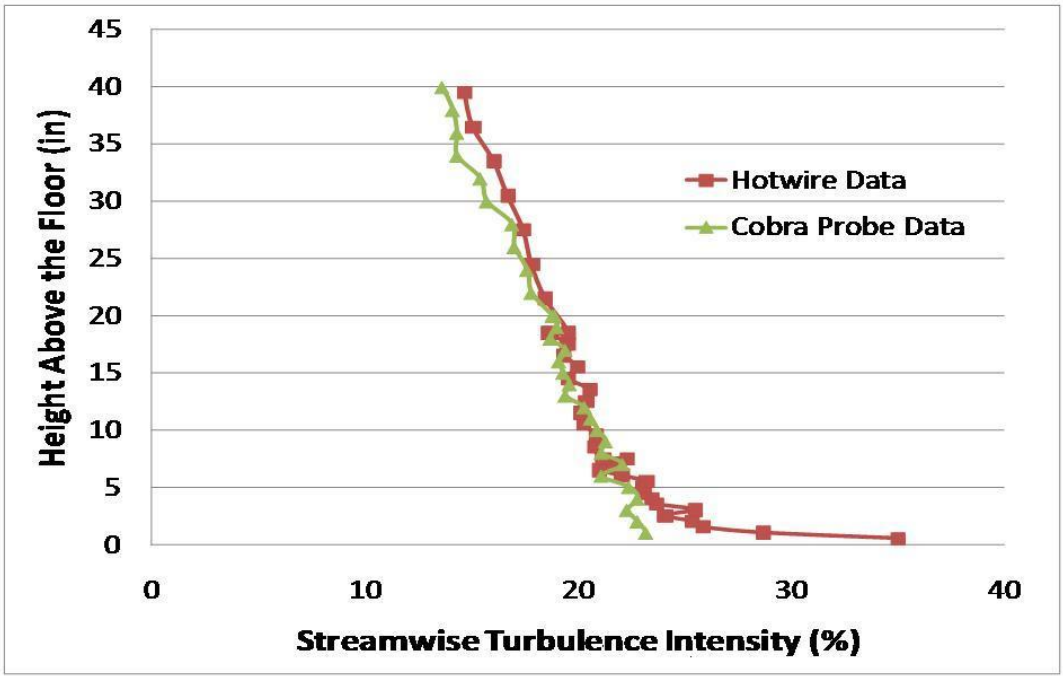

Figure 4.6 Streamwise turbulence intensity profiles

gap ($1 - 2$ mm) was maintained between the floor of the wind tunnel and the building models and all around the aluminum rod in the floor. All the force data were obtained using this type of setup.

4.3 Data Acquisition and Analysis

A sampling time had to be determined over which data were averaged for steady state results before testing could begin. Turbulent flow requires longer sampling times to maintain stationary statistics. An initial test was performed to determine an adequate sampling time. The results of this study can be seen in Figure 4.9. From the figure, the averaged value was steady beyond 100 seconds. Therefore, a sampling time of 120 seconds was used for all load measurements.

The Reynolds number is an important parameter in the study of fluid dynamics. The Reynolds number (Equation 4.2) is the ratio of inertial forces to viscous forces.

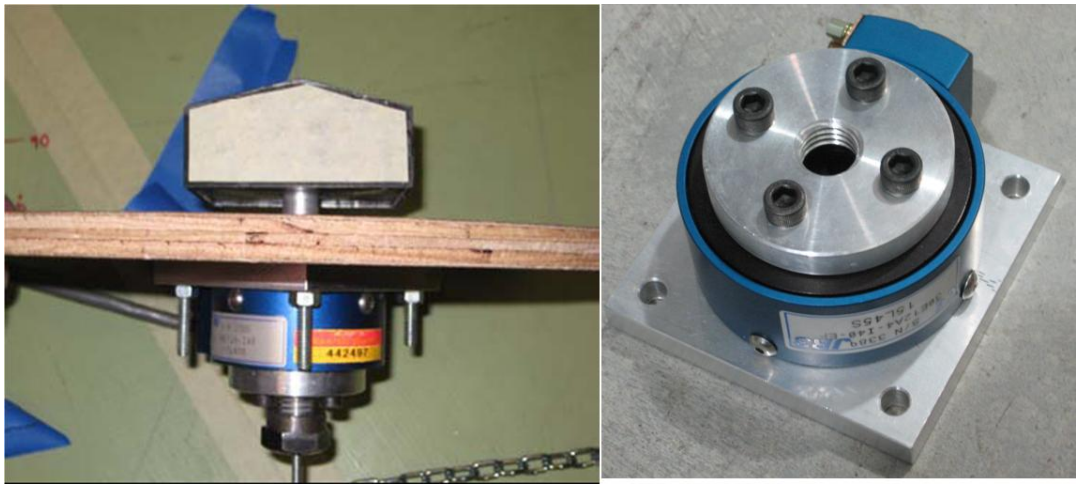

Figure 4.7 The JR3 multi-axis force sensor and cantilever model setup

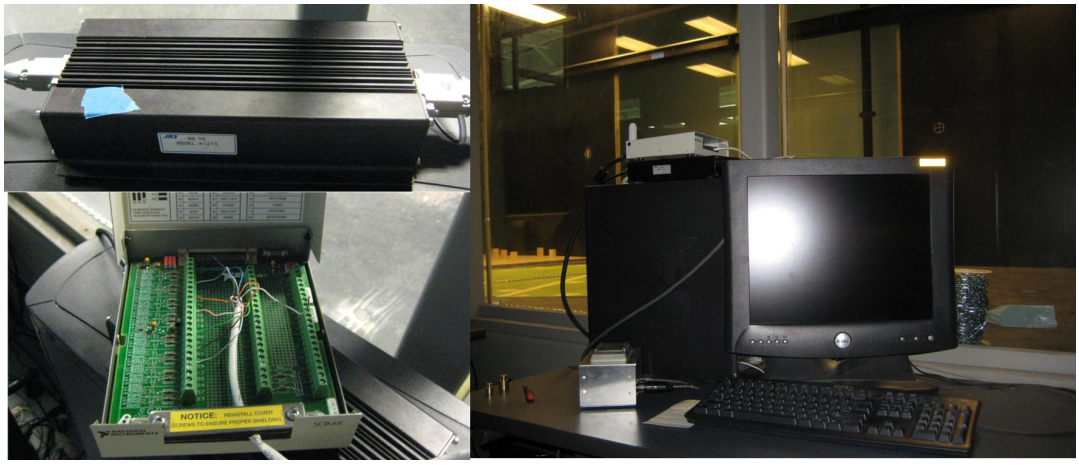

Figure 4.8 JR3 data acquisition system setup and components

$$Re = \frac{\rho \nu L}{\mu} \tag{4.2}$$

It is a non-dimensional parameter to determine dynamic similitude between two flows of similar flow pattern. The Reynolds number can be used to determine the appropriate flow pattern around a body. For example, for Reynolds number equal to one, the flow around a circular cylinder remains attached and follows potential theory. As the Reynolds number increases the flow separates, and a wake is formed behind

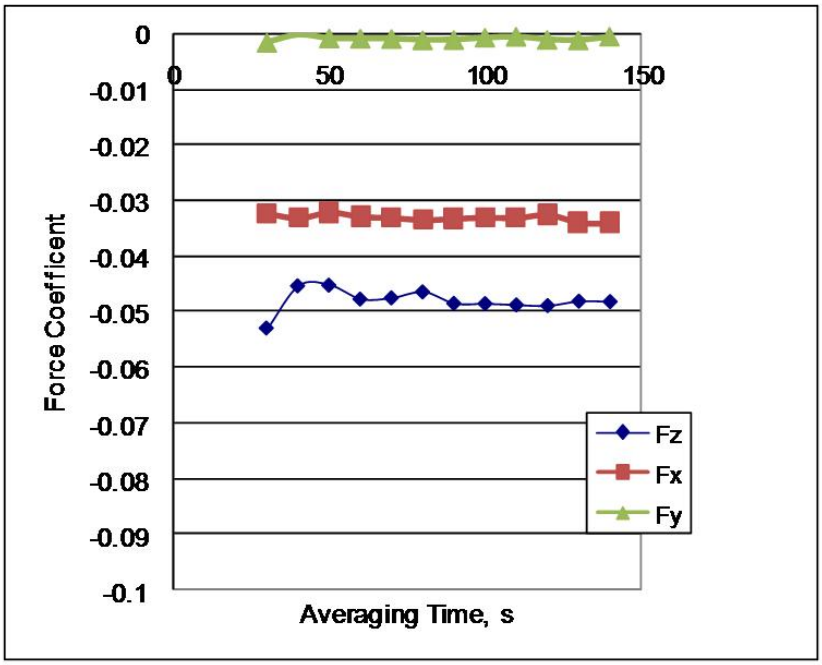

Figure 4.9 Graphical results of JR3 steady data test

the cylinder. This changes the pressure distribution around the cylinder and increases the form drag. Bluff bodies with sharp corners, however, are independent of Reynolds number effects. A sharp corner will always cause separation regardless of the wind speed. For the present study, Reynolds number dependency was investigated to determine if testing should be performed at multiple velocities. The results of this test are presented in Figure 4.10.

From the plots, it can be seen that the force coefficients remained almost the same at three different velocities, $27.2\frac{ft}{s}$, $42.0\frac{ft}{s}$, and $54.8\frac{ft}{s}$. The Reynolds number had a very little effect in the range of Reynolds numbers tested (2.1×10^4 - 4.3×10^4) on the characteristics of the flow. Therefore, this study was carried out only at one wind speed, and all load values were converted into non-dimensional force coefficients. All load measurements in this study were taken at a wind tunnel motor frequency of 15 Hz corresponding to a wind speed of 42 $\frac{ft}{s}$ at a height of 3.96 in. from the test section floor in the boundary layer measured at the center of the model. This height corresponds to a

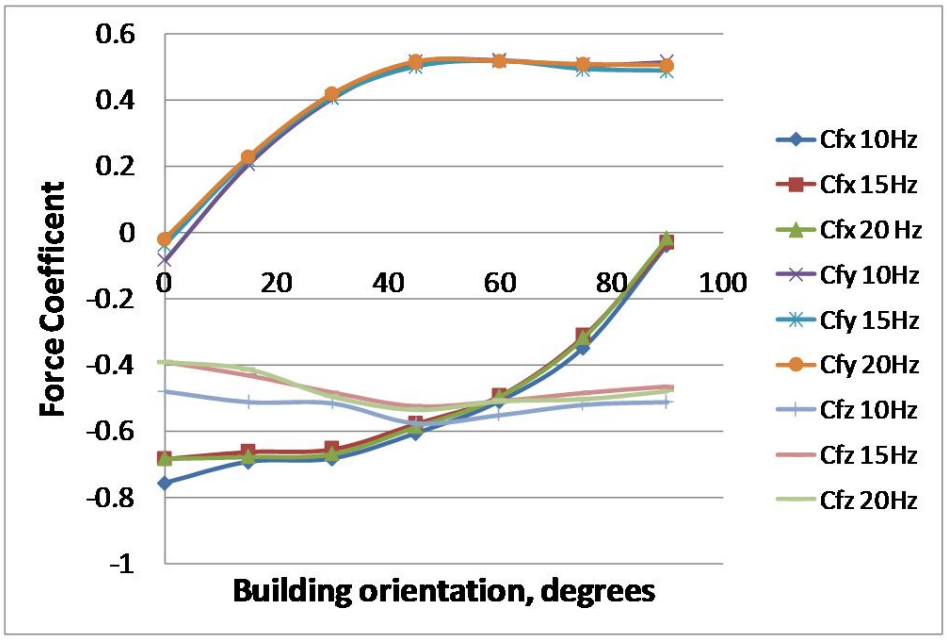

Figure 4.10 Reynolds number effects on the 15° gable roof base model

full-scale reference height (33 ft.) that is commonly used in atmospheric boundary layer wind. This wind speed (V_∞) was used in calculating the non-dimensional mean force coefficients (Equation 4.3) and the peak force coefficients (Equation 4.4).

$$C_{F_x} = \frac{F_x}{q_\infty A_x}, \quad C_{F_y} = \frac{F_y}{q_\infty A_y}, \quad C_{F_z} = \frac{F_z}{q_\infty A_z}, \quad q_\infty = \frac{1}{2}\rho_\infty V_\infty^2 \tag{4.3}$$

In Equation 4.4, $C_{F_x^{max}}$, $C_{F_y^{max}}$, and $C_{F_z^{max}}$ are the peak force coefficients corresponding to peak forces(F_x^{max}, F_y^{max},F_z^{max}) that occurred during the 120 second time series.

$$C_{F_x^{max}} = \frac{F_x^{max}}{q_\infty A_x}, \quad C_{F_y^{max}} = \frac{F_y^{max}}{q_\infty A_y}, \quad C_{F_z^{max}} = \frac{F_z^{max}}{q_\infty A_z}, \quad q_\infty = \frac{1}{2}\rho_\infty V_\infty^2 \tag{4.4}$$

The reference areas (A_x, A_y, A_z) used in the coefficients can be seen in Figure 4.11.

The air density (ρ_∞) used in Equations 4.3 and 4.4, was calculated for moist air as given by Bolton (1980). Water vapor reduces the density of air, because the molecular

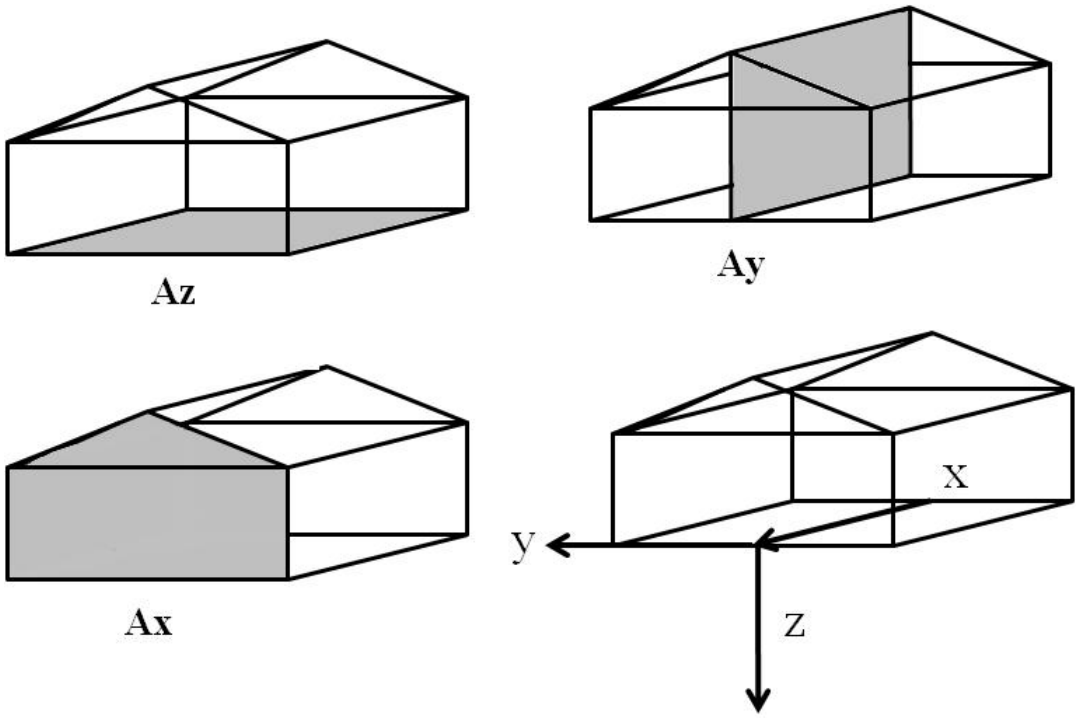

Figure 4.11 Model projected areas and model axis used during experiments

mass of water is less than the molecular mass of air. The total number of molecules in a volume is constant for any gas (ideal gas law) at a constant value of temperature and pressure. Therefore, a volume of moist air has the same number of molecules as a volume of dry air, but the water molecules weigh less reducing the overall mass per volume (density). The following equations were used to calculate the density of air inside the wind tunnel during the experiment. The variables used in the equations are the barometric pressure (B(torr)) in torr, vapor pressure (e) in torr, density (ρ_∞, ρ_{dryair}) of the moist air and dry air, and temperature ($T(^\circ F)$, $T(^\circ C)$, $T(K)$) in degrees Fahrenheit, degrees Celsius, and Kelvin.

$$T(^\circ C) = \frac{5}{9}(T(^\circ F) - 32), \qquad e = \frac{RH\%}{100\%}[6.112 \ exp(\frac{17.67(T(^\circ C))}{T(^\circ C) + 243.5})] \tag{4.5}$$

$$T(K) = T(^{\circ}C) + 273.15, \qquad \rho_{\infty} = (\frac{273.13}{T(K)})[\frac{B(torr) - 0.3783e}{760}]\rho_{dryair} \tag{4.6}$$

$$1.333mb = 1torr, \qquad 1\frac{Kg}{m} = 0.60243\frac{lb}{ft^3}, \qquad \rho_{dryair} = 1.25\frac{kg}{m^3} \tag{4.7}$$

The data was taken with 500 Hz sampling rate. The mean and peak force coefficients were calculated for each model at all building orientations using Equations 4.3 and 4.4. The buildings were tested for seven orientations with respect to the wind, 0, 15, 30, 45, 60, 75, and 90 degrees (θ defined in Figure 4.12).

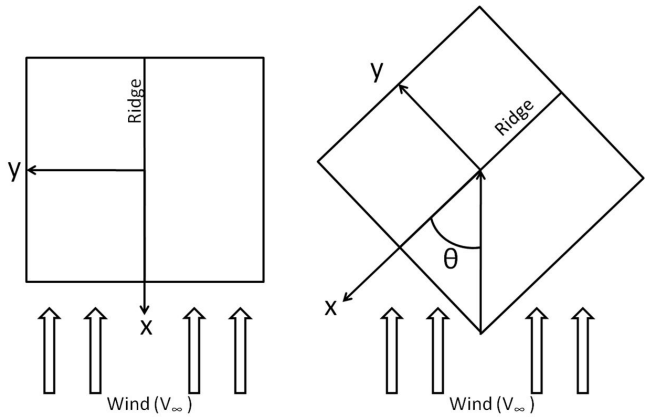

Figure 4.12 Building orientation (θ) used during experiment

Initial testing was conducted to provide statistical verification of the accuracy and consistency of the force sensor output because the expected force values were less than 1% of the capacity of the force sensor. The objective of this testing was to determine the standard deviation of the peak and mean force coefficients for a set of 20 data runs. Two buildings at two different orientations were used during testing. The gable base model was tested at 0 and 60 degrees and the flush edge spoiler model was tested at 60 and 90 degrees. These angles correspond to the occurrence of the largest mean and peak force coefficients. The test conditions for this set of tests were the same as described in this section. Let σ_m be the standard deviation of the mean force coefficients of all 20

	Er_m	Er_p
C_{F_x}	6%	16%
C_{F_y}	4%	15%
C_{F_z}	6%	14%

Table 4.1 Error due to random deviation of data

data runs and σ_p be the standard deviation of the peak force coefficients of all 20 data runs. From this testing, it was determined with a 95% confidence level that the mean force coefficients for all three orthogonal axes were within $\pm 2\sigma_m$ (Equation 4.8) and the peak force coefficients for all three orthogonal axes were within $\pm 1.5\sigma_p$ (Equation 4.9).

$$\overline{C_F} - 2\sigma_m \leq C_F \leq \overline{C_F} + 2\sigma_m \tag{4.8}$$

$$\overline{C_{F^{max}}} - 1.5\sigma_p \leq C_{F^{max}} \leq \overline{C_{F^{max}}} + 1.5\sigma_p \tag{4.9}$$

C_F and $C_{F^{max}}$ are the individual values of mean and peak force coefficients for each data run, and $\overline{C_F}$ and $\overline{C_{F^{max}}}$ are the averaged values of C_F and $C_{F^{max}}$ for all data runs. The maximum percent errors in the mean force coefficient (Er_m) and peak force coefficient (Er_p) associated with the random deviation of the values from the mean can be calculated using Equations 4.10 and 4.11. The largest values of Er_m and Er_p of all tests for the three force coefficients are tabulated in Table 4.1.

$$Er_m = \frac{2\sigma_m}{\overline{C_F}} \times 100 \tag{4.10}$$

$$Er_p = \frac{1.5\sigma_p}{\overline{C_{F^{max}}}} \times 100 \tag{4.11}$$

The comparison tests began once the initial testing and calibration of the data acquisition equipment was complete. The tunnel was run at a constant speed and data

were collected for 120 seconds for each record and each force value was averaged over a set of three runs to reduce sampling error in the data. The gable base model was tested first followed by 10 different mitigation models. Labview was used to record the data for all three components of force. Labview displayed and recorded the following information; mean force, rms force, and the force time series. The mean force and force time series data were exported into Excel. Excel was used to evaluate the data and develop the graphs for the mitigation model comparison. The gable base model and the tunnel velocity at 3.96 in height in the boundary layer were checked periodically to insure consistency in the data. This check ensured that an accurate comparison was maintained.

CHAPTER 5 RESULTS AND DISSCUSION

All the wind tunnel test results are summarized in this chapter. The large amount of wind tunnel data that were collected required a specific method to organize a direct comparison between all the models. A simple parameter is proposed here for comparison that will be referred as the performance index. The performance index is calculated for each building orientation and then averaged over all building orientations. The purpose of the performance index is that it eliminates the need to compare individual building orientations and all three components of force. Before the performance index is defined, the three component force coefficient results can be to be simplified into two components, a lift force coefficient (C_{F_L}) and a shear force coefficient (C_{F_S}). Equations 5.1 and 5.2 define the lift and shear force coefficients in terms of the previously defined force coefficients in the orthogonal coordinate system (Figure 4.11).

$$C_{F_L} = -C_{Fz} \tag{5.1}$$

$$C_{F_S} = \sqrt{C_{Fx}^2 + C_{Fy}^2} \tag{5.2}$$

Ip_{SL} (Equation 5.3) is the overall average performance index of all building orientations for both lift and shear force coefficient (C_{F_L} and C_{F_S}). The performance index is used for comparison with the gable base model. Ip_{SL}^{max} (Equation 5.4) provide a similar averaged performance index but for the peak lift and peak shear force coefficients ($C_{F_L^{max}}$ and $C_{F_S^{max}}$) instead of the mean force coefficients.

$$Ip_{SL} = \frac{1}{2}\left(\frac{C_{F_S}^{Gable}}{C_{F_S}^{Model}} + \frac{C_{F_L}^{Gable}}{C_{F_L}^{Model}}\right) \tag{5.3}$$

$$Ip_{SL}^{max} = \frac{1}{2}\left(\frac{C_{F_S^{max}}^{Gable}}{C_{F_S^{max}}^{Model}} + \frac{C_{F_L^{max}}^{Gable}}{C_{F_L^{max}}^{Model}}\right) \tag{5.4}$$

The performance index mathematically represents how many times larger the load on the gable roof is than the modified model. They cannot be used as a exact representation of how many times smaller the modified model loads are than the gable base model. They are used only to provide a comparison of performance not exact load reduction. The percent reduction of force coefficient (Equation 5.5) will be used in the discussion to show the percent difference in the shear and lift force coefficients. A positive value means a reduction in force coefficient and a negative value means an increased force coefficient compared to the gable base model. The percent difference will be displayed using bar graphs (Appendix A D) and the performance index will be displayed using bar graphs in Chapter 5.

$$\%\, difference = \frac{C_{F^{Gable}} - C_{F^{Model}}}{C_{F^{Gable}}} \times 100 \tag{5.5}$$

5.1 Effect of Aerodynamic Modification

The mean force coefficient plots can be seen in Figures A.1 and A.2. The aerodynamically modified models tend to improve the loads compared to the gable base model; all average performance indices are greater than 1 (Figure 5.1). The variable sloped roofs (VISR and VDSR) decreased the shear force coefficients, but not as effectively as the hip and curved corners model. The largest average performance index of the lift force coefficient was accomplished by the VISR model which had a 14.3% reduction (Figure A.4). The VDSR model did not provide useful mitigation of lift force coefficient but did provide a 10.7% reduction in shear force coefficient (Figure A.3). The average performance index of the variable sloped roofs were about the same (Figure 5.1). The curved

corner model could not outperform the hip base model. It provided 20.6% reduction in the shear force coefficient compared to 23.9% for the hip base model. The curved corner model and the hip base model had little effect on lift. The hip base model had the largest average performance index of 1.181, mostly due to a 23.9% reduction of the shear force coefficients.

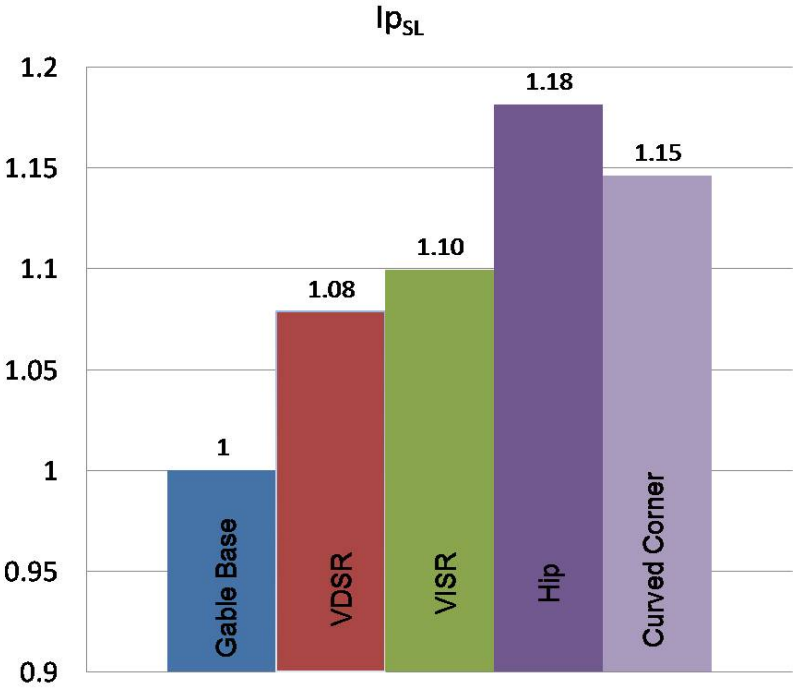

Figure 5.1 Ip_{SL} comparison of aerodynamic modification models

The peak force coefficient plots can be seen in figures A.5 and A.6. The aerodynamically modified models, which focus on peak lift load mitigation, tend to increase the peak shear loads, but the models such as hip base and curved corner models, which focus on peak shear load mitigation tend to increase the peak uplift. The VISR model was the only model that provided peak lift mitigation (7.4% reduction as in Figure A.8). The hip and curved corner models were the only models that provided peak shear load reduction, 12.8% and 3.1%, respectively (Figure A.7). The hip roof had the largest average performance index of 1.058 (Figure 5.2).

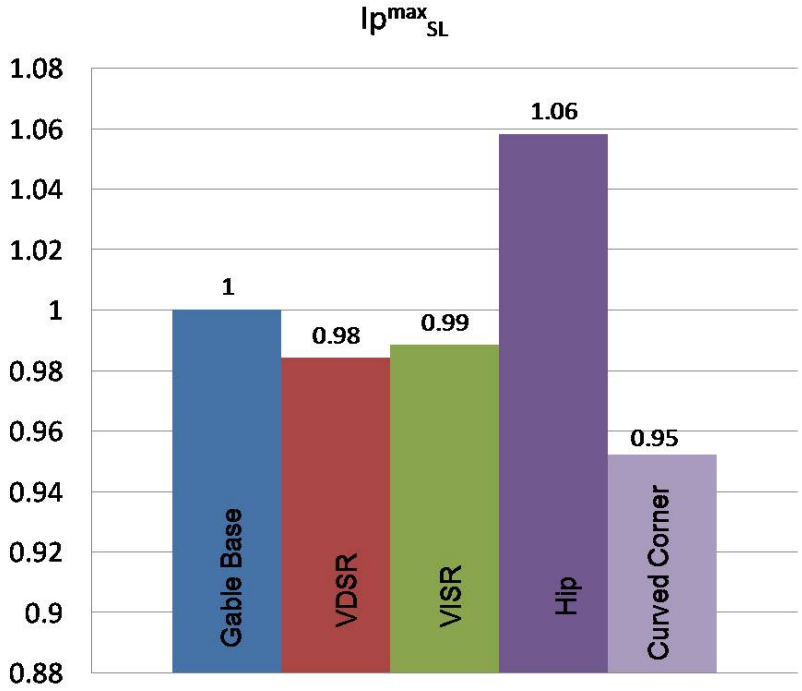

Figure 5.2 Ip_{SL}^{max} comparison of aerodynamic modification models

5.2 Effect of Aerodynamic Adaptation

5.2.1 Aerodynamic Roof Attachment

The mean force coefficient plots can be seen in figures B.1 and B.2. The aerodynamic attachments tend to improve the overall loading compared to the gable base model. From Figure B.4, the edge spoiler model that is flushed with the building provides more uplift mitigation than the attachment that overhangs. The porous canopy roof model (PCR) with 10% porosity provides more uplift mitigation than the PCR model with 1% porosity. From Figure B.3, the flush edge spoiler provides more shear load reduction than the overhang edge spoiler model. The 1% PCR model provides more reduction in the shear loads than the 10% PCR. The flush edge spoiler model has the largest uplift mitigation of 32.3% reduction. The 10% PCR model had the second largest reduction of 31.1%. The 1% PCR model and the flush edge spoiler model had the most shear

load reduction of 7.9% and 6.9% respectively. From Figure 5.3, the flush edge spoiler model has the best overall averaged performance index of 1.276, followed by the 10% PCR model with 1.233.

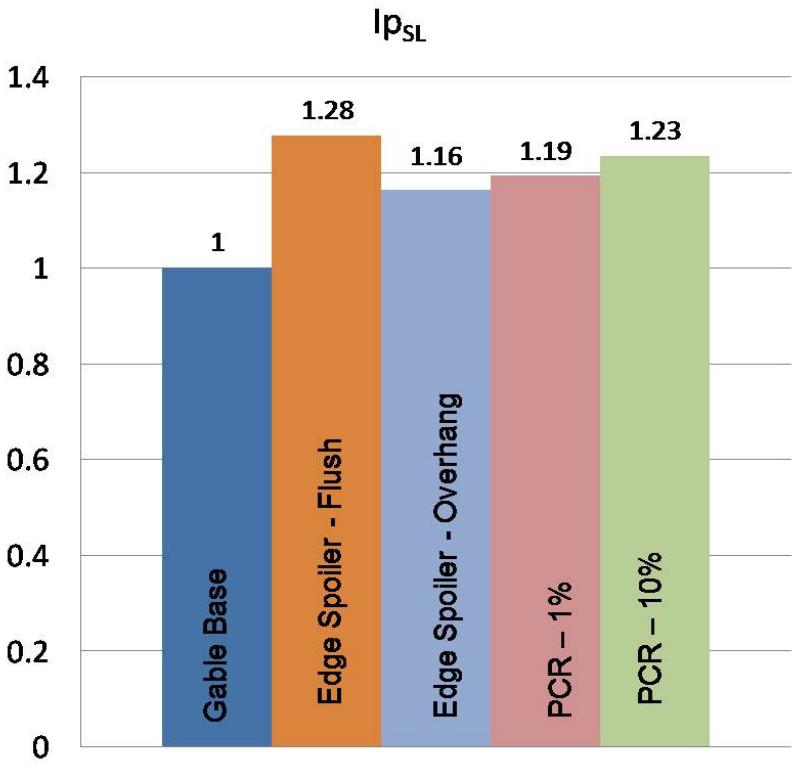

Figure 5.3 Ip_{SL} comparison of aerodynamic adaptation models

The peak force coefficient plots can be seen in B.5 and B.6. The aerodynamic attachments tend to reduce the peak uplift at the cost of increasing the peak shear loads. From figure B.8, the flush edge spoiler model has the largest reduction of 26.7% in peak lift coefficient, followed by the 10% PCR model with a reduction of 22.3%. From Figure B.7, the flush edge spoiler model increases the peak shear loads by 6.9%. The 1% PCR and 10% PCR models increase the peak shear loads by 6.6% and 11%, respectively. From Figure 5.4, the flush edge spoiler model had the best averaged performance index of 1.150.

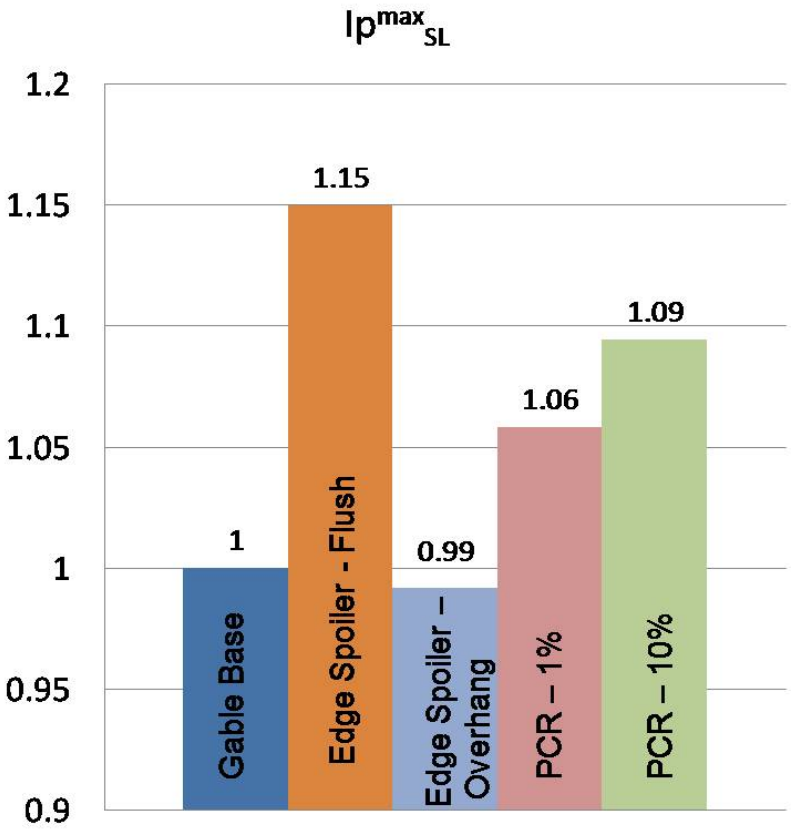

Figure 5.4 Ip_{SL}^{max} comparison of aerodynamic adaptation models

5.2.2 Passive Pressure Equalization

The mean force coefficient plots can be seen in Figures C.1 and C.2. The passive pressure equalization method does not have a great effect on the shear force, but offers significant lift force coefficient reduction. From Figure C.4, the roof passive pressure equalization (PPE) method reduced the lift force coefficient by 31.4%, while the wall PPE reduced the lift force coefficient by 6.5%. From Figure C.3, the roof PPE (8.8% reduction) outperformed the wall PPE (6.8% reduction). It seems the wall PPE is not an efficient method to reduce the shear loads, which is inefficient because at a building orientation of 0° the separation around the building causes the transverse loads (F_y) on each side of the building to oppose each other causing a cancellation effect. At a building

orientation of 90° the longitudinal loads (F_x) have the same effect. This cancelation reduces the effectiveness of the method at these orientations rendering half of the suction useless. At other building orientations the suction on the windward side is not strong enough to reduce suction on the leeward side. The shape of the separation bubble is unchanged and the form drag is not reduced. The roof PPE produced significant reductions in the uplift and sufficient reductions in the shear load. From Figure 5.5, the averaged performance index of the roof PPE was 1.277. The reduction in the separation over the roof resulted in a reshaping of the separation bubble, therefore reducing the drag slightly. The roof PPE model provides an effective method to reduce the mean force coefficients.

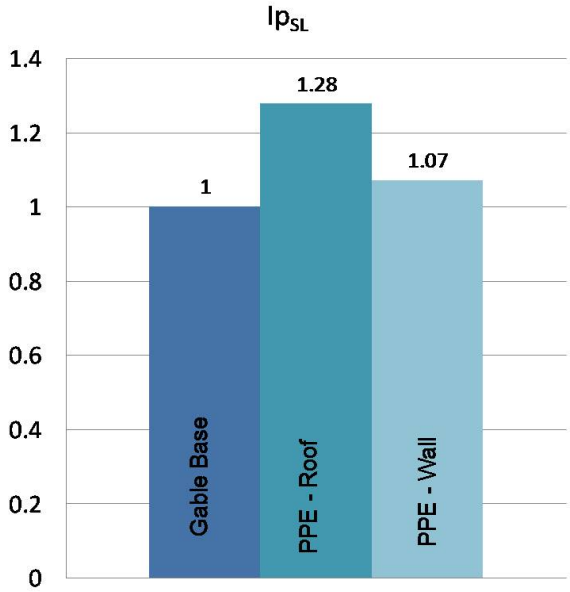

Figure 5.5 Ip_{SL} comparison of passive pressure equalization models

The peak force coefficient plots can be seen in Figures C.5 and C.6. The passive pressure equalization method provided no significant peak shear load reduction. From Figure C.8, the roof PPE method had a 16% reduction in the peak lift force coefficient, whereas the wall PPE provided no significant change in the peak lift force coefficient.

From Figure C.7, the roof PPE had a 10.2% increase in the peak shear loads, and the wall PPE provided a 1.5% reduction. From Figure 5.6, the average performance index of the roof PPE and the wall PPE was 1.049 and 1.002 respectively. The roof PPE is only efficient at reducing the peak uplift loads.

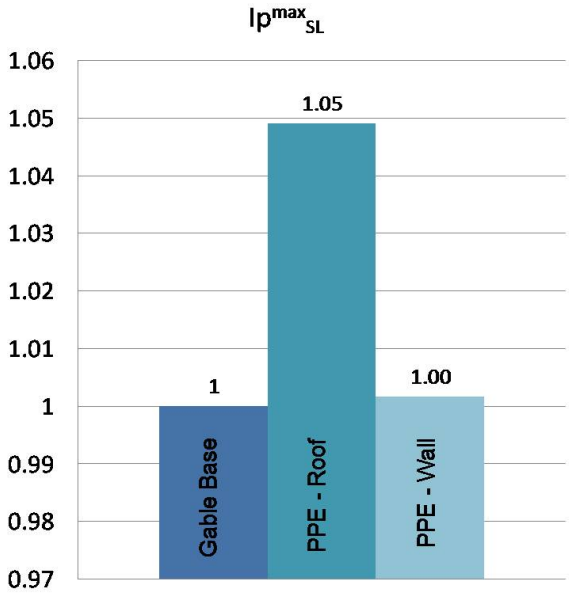

Figure 5.6 Ip_{SL}^{max} comparison of passive pressure equalization models

5.3 Comparison of Mitigation Methods

The mean force coefficient plots for all models tested can be seen in Figures D.1 and D.2. The trends of the plots show that the largest uplift occurred for most models at building orientation of 60°. Figure D.2 shows that when the wind is oriented parallel to the ridge of the roof ($\theta = 0°$), the uplift is smaller than when the wind is oriented perpendicular to the ridge ($\theta = 90°$). From Figure D.1, the shear force has the opposite effect. When the wind is parallel to the ridge the shear force is larger than when the wind is perpendicular to the ridge. The reason for this is the projected area in the flow is larger for wind parallel to the ridge than when the wind is perpendicular to the ridge.

This increase in projected area increases the drag of the model, therefore increasing the shear force on the building. The largest mean shear forces occur between 30° and 60°. To determine the worst wind loads on a building through load measurements, a building orientation of around 60° would provide the largest values compared to testing at every 15° increments used in this study.

The primary goal of this study was to determine a useful method to reduce the wind loads on a roof. From Figure D.4, the models which showed significant uplift mitigation were the flush edge spoiler, roof PPE, and the 10% PCR with 32.3%, 31.4%, and 31.1% reduction, respectively. From Figure D.3, the models which showed significant shear load mitigation were the hip base model and the curved corner model with 23.9% and 20.6% respectively. From Figure 5.7, the best overall averaged performance was accomplished by the flush edge spoiler, roof PPE, and the 10% PCR models with 1.276, 1.277, and 1.233, respectively.

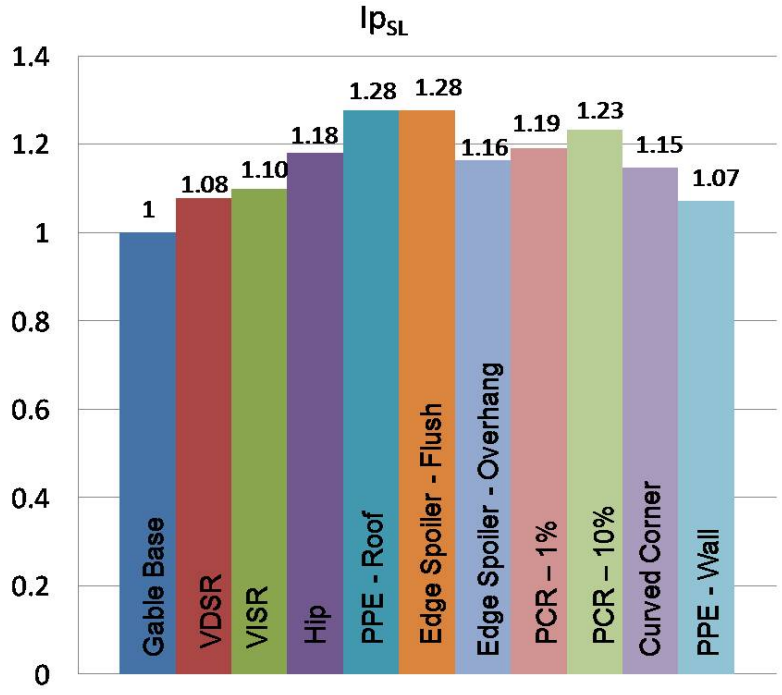

Figure 5.7 Ip_{SL} comparison of all mitigation models

Model Type	$\theta_{C_{F_L^{max}}^{max}}$	$C_{F_L^{max}}^{max}$	$\theta_{C_{F_L}^{max}}$	$C_{F_L}^{max}$	Factor
15° Gable	60	1.433	60	0.392	3.659
VDSR	60	1.491	60	0.385	3.871
VISR	60	1.353	45	0.359	3.771
Hip	15	1.553	60	0.372	4.172
PPE - Roof	60	1.193	60	0.276	4.331
Edge Spoiler - Flush	90	1.196	60	0.270	4.429
Edge Spoiler - Overhang	90	1.573	60	0.309	5.089
PCR - 10%	90	1.414	45	0.300	4.712
PCR - 1%	90	1.190	60	0.273	4.363
Curved Corner	60	1.600	60	0.390	4.104
PPE - Wall	60	1.586	60	0.373	4.254

Table 5.1 Maximum mean and peak uplift loads

The peak force coefficient plots for all models tested can be seen in Figures D.5 and D.6. The values of the longitudinal peak force coefficient ($C_{F_x^{max}}$) at 90° and the transverse peak force coefficient ($C_{F_y^{max}}$) at 0° do not go to zero. The peak values are taken at an instance in time, therefore the opposing forces are not of the same magnitude. The reason for this mismatch is because of the random turbulence in the boundary layer wind. The peak lift force coefficient for most models still had a maximum at 60° building orientation. The roof attachment models seem to have skewed the maximum peak force coefficient to occur at 90°.

Table 5.1 shows the building orientation at which the maximum peak lift force coefficient occurred, the maximum peak lift force coefficient ($C_{F_L^{max}}$), the maximum mean lift force coefficient (C_{F_L}), and the factor by which the peak force coefficient is larger than the mean force coefficient for each model. The table shows that the peak values are 3.6 times larger than the mean values for the gable base model. The table also shows that the multiplication factor between the peak and the mean values is greater for all mitigation models. This shows that the mitigation methods reduce the mean loads more efficiently than the peak loads.

Figure D.8 shows that the flush edge spoiler, 10% PCR, and roof PPE methods offer the most uplift reduction with values of 26.7%, 22.3%, and 16%, respectively. From Figure D.7, the hip roof is the only model to provide any significant peak shear force coefficient reduction (12.8%). The averaged peak force performance (Figure 5.8) is less than the averaged mean load performance for all models. The largest values were for the flushed edge spoiler and the 10% PCR models with values of 1.15 and 1.094, respectively. Once again this reiterates the fact that the mitigation methods are less efficient in peak load mitigation.

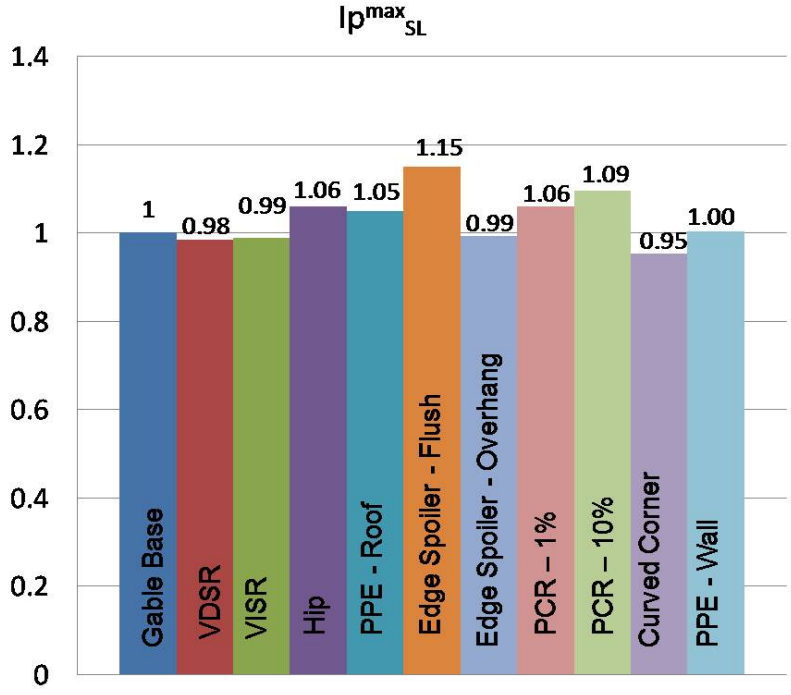

Figure 5.8 Ip_{SL}^{max} comparison of all mitigation models

CHAPTER 6 SUMMARY, CONCLUSIONS, AND FUTURE WORK

6.1 Summary and Conclusions

The research in this thesis is purely a comparative study; no attempt has been made to relate load results to pressure measurement or to field test. The traditional gable roof was compared to ten new designs which focused on aerodynamically modified roof shapes or externally added device to the existing roof. The results showed that the edge spoiler, the porous canopy roof, the variable sloped roofs, and passive pressure equalization provided wind-induced uplift load mitigation. The models with curved corners and hip roof provided shear load mitigation in high winds. Mean uplift load reductions of over 30% and shear load reduction of over 20% are possible with some of these methods. The largest mean lift force coefficients occurred at 60° and the largest mean shear force coefficients occurred between 30° and 60°. The largest peak uplift force coefficient occurred at 60°, except the roof attachment models and the hip roof. The roof attachment models saw the largest peak uplift force coefficient at a building orientation of 90°. The hip roof model saw the largest peak uplift force coefficient at a building orientation of 15°. Overall the methods had a tendency to reduce the mean lift force coefficient more effectively than the peak lift force coefficients. The edge spoiler proved to outperform the other methods in uplift load mitigation. This method should have relatively low material and implementation cost because of its simplistic design compared to some of the other methods considered for residential buildings. The porous

canopy roof and passive pressure equalization methods also would provide adequate load mitigation, but create many design and implementation issues which need to be resolved before they can become a commercial product. These would require more construction material to build increasing the cost of implementation. The problems associated with these methods, coupled with the fact that their performance was less than the edge spoiler method, lowers the benefits that these methods could offer for residential buildings.

6.2 Future Work

This study was a preliminary investigation to explore possible techniques that could provide wind load mitigation for residential one-story gable roof buildings with the goal that similar techniques can be generally used across all low-rise buildings. The continuation of this study could include the following suggestions.

- The effect of momentum injection − A model utilizing a rotating cylinder along the ridge of the gable roof was built in the current study and ready for the wind tunnel testing.

- The effect of tangential boundary layer blowing − This method re-energizes the low momentum boundary layer by passively taking air from one location and injecting it into the separation bubble tangentially to the surface.

- The effect of combining methods − Most of the methods saw significant uplift mitigation at the cost of increased shear load. The edge spoiler, porous canopy roof, and variable increasing sloped roof methods can be combined with the hip or curved corner models to improve the performance.

- The effect of complex terrain − The influence of various sized hills, valleys, and

gentle slopes on the suburban boundary layer flow and its effects on the effectiveness of these methods should be studied.

- The effect of surrounding buildings − A residential community is comprised of many surrounding structures. The proximity of other building in relation to the test building will affect the flow around the building. This should be studied in relation to the suggested techniques.

- Particle Image Velocimetry − A PIV study can be used to visually understand the flow pattern and the vortex structure around the modified buildings. This will provide a better understanding of the mechanics of each method and also provide insight to any improvements which can be made.

APPENDIX A RESULTS OF AERODYNAMICALLY MODIFIED MODELS

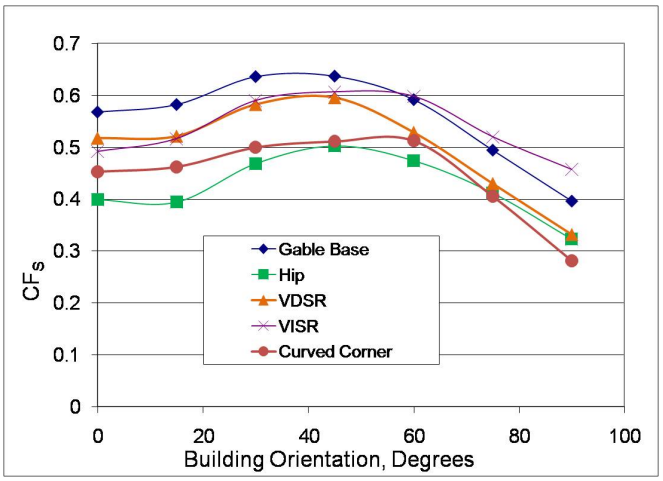

Figure A.1 Mean shear force coefficient plot

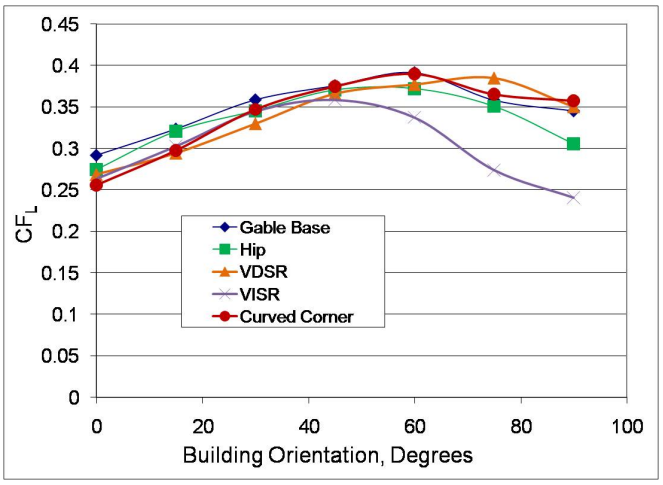

Figure A.2 Mean lift force coefficient plot

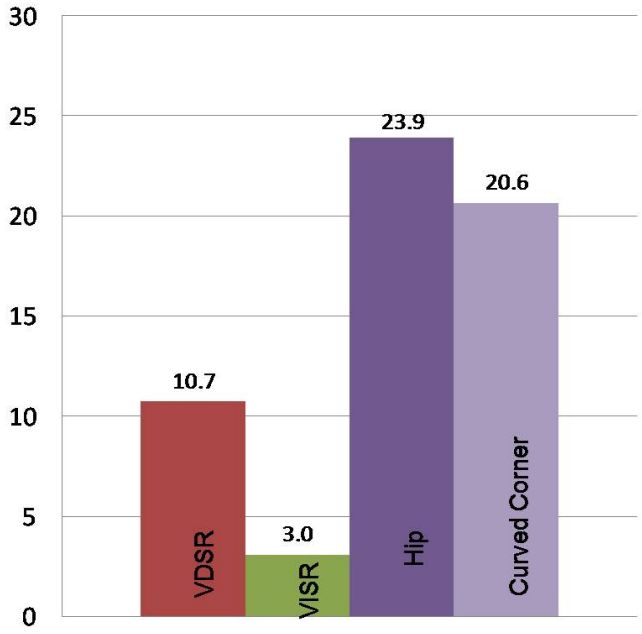

Figure A.3 Percent difference of mean shear force coefficient

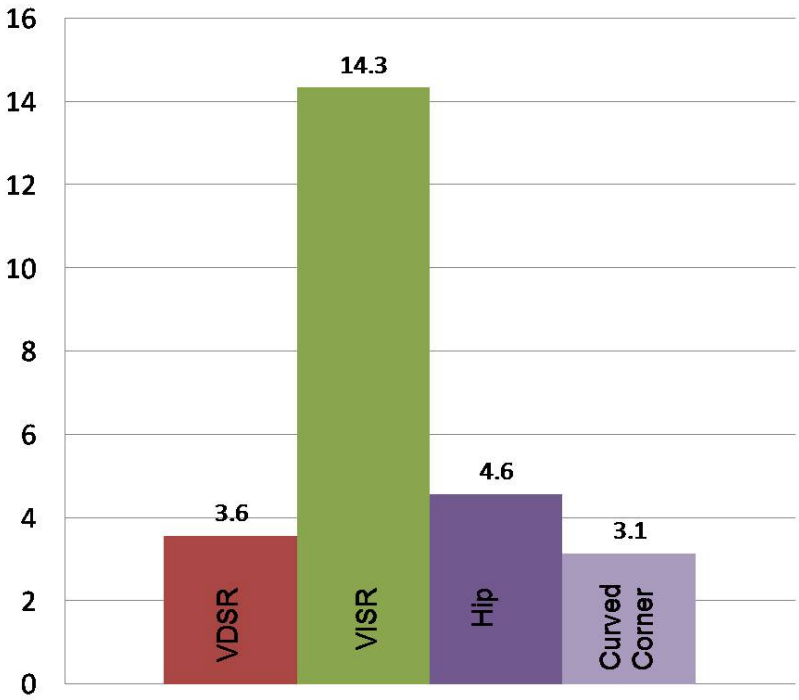

Figure A.4 Percent difference of mean lift force coefficient

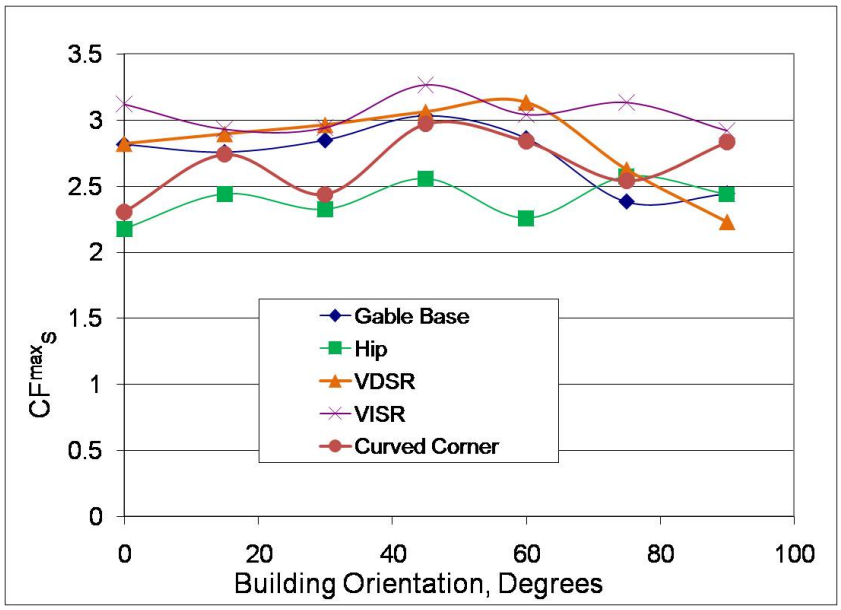

Figure A.5 Peak shear force coefficient plot

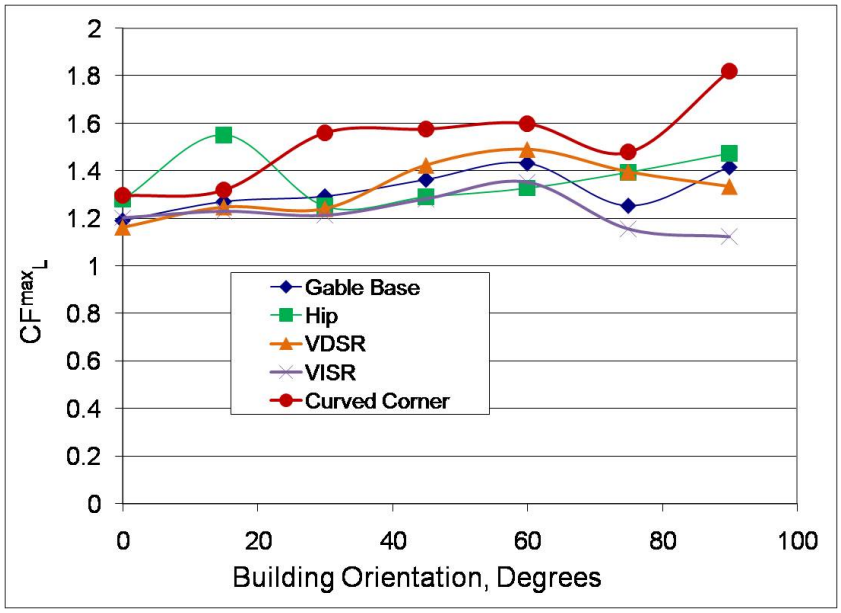

Figure A.6 Peak lift force coefficient plot

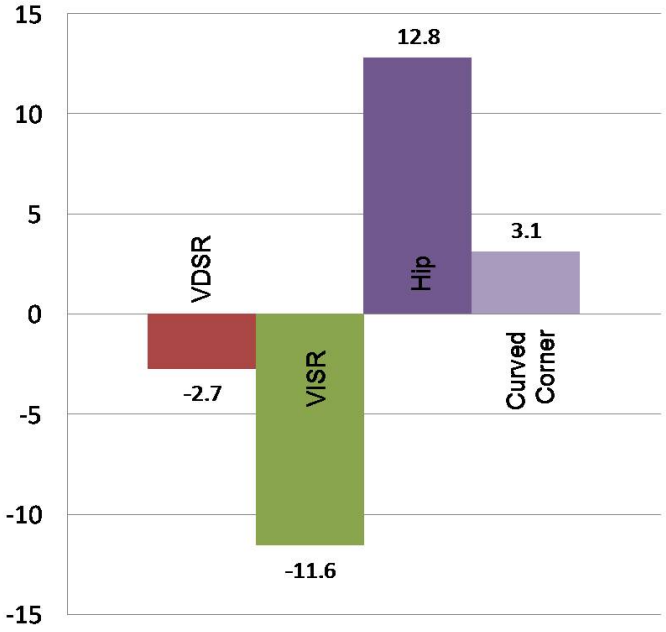

Figure A.7 Percent difference of peak shear force coefficient

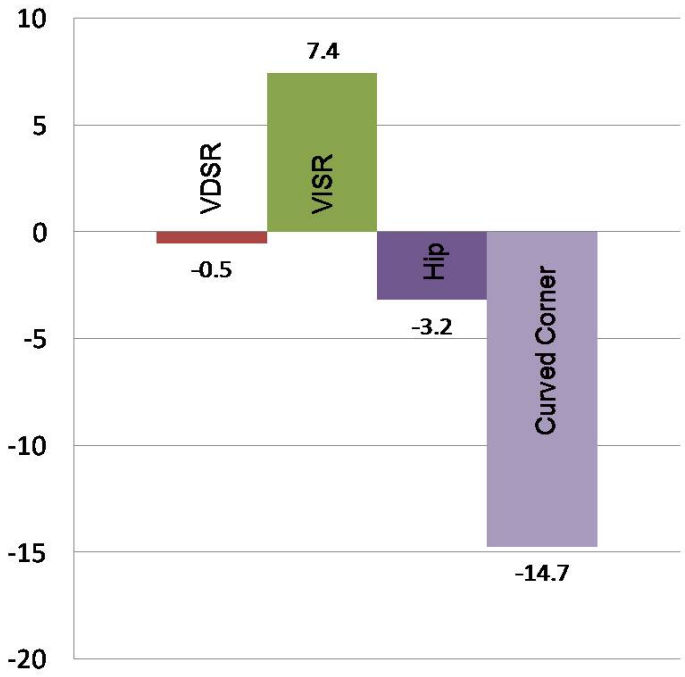

Figure A.8 Percent difference of peak lift force coefficient

APPENDIX B RESULTS OF AERODYNAMICALLY ADAPTED MODELS

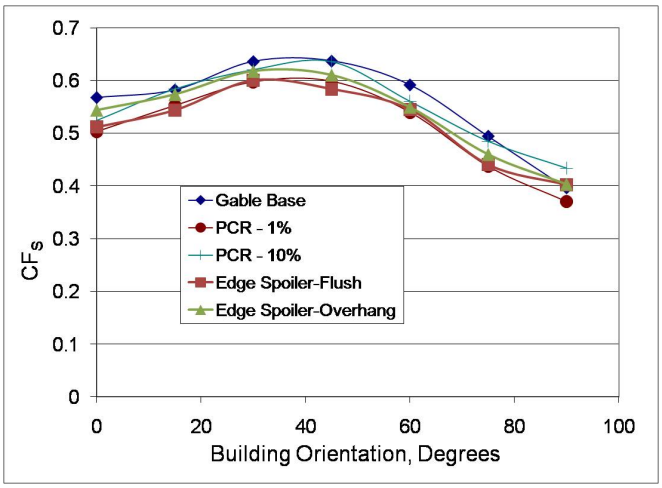

Figure B.1 Mean shear force coefficient plot

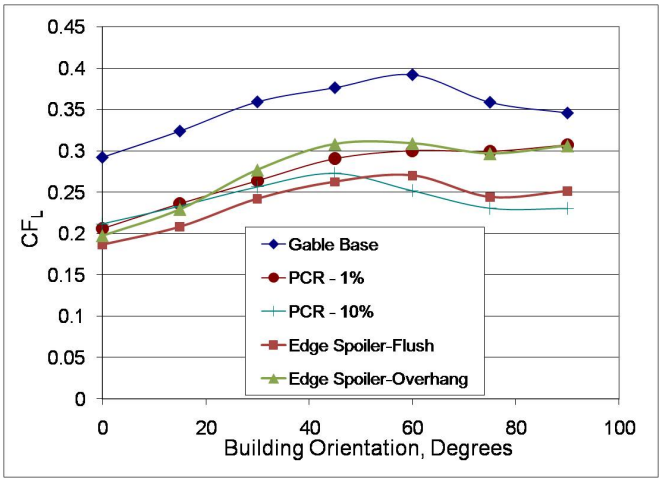

Figure B.2 Mean lift force coefficient plot

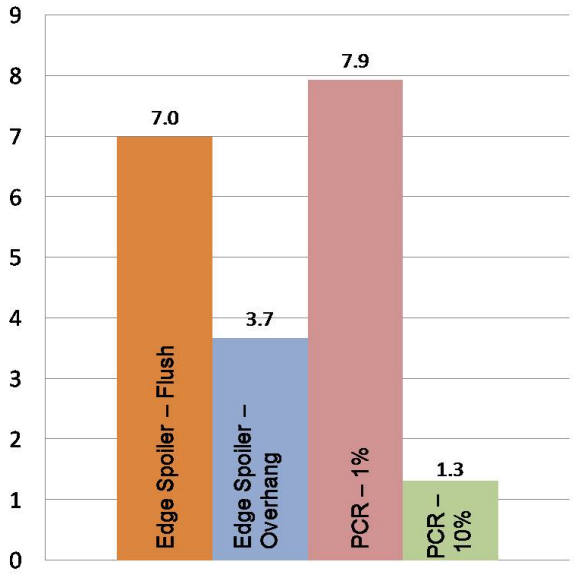

Figure B.3 Percent difference of mean shear force coefficient

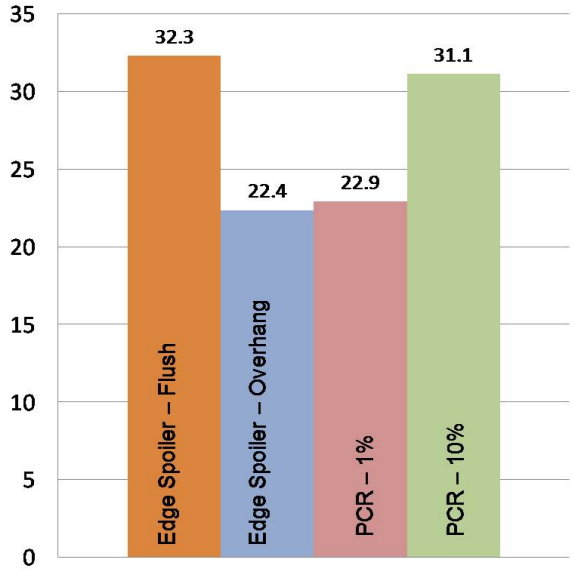

Figure B.4 Percent difference of mean lift force coefficient

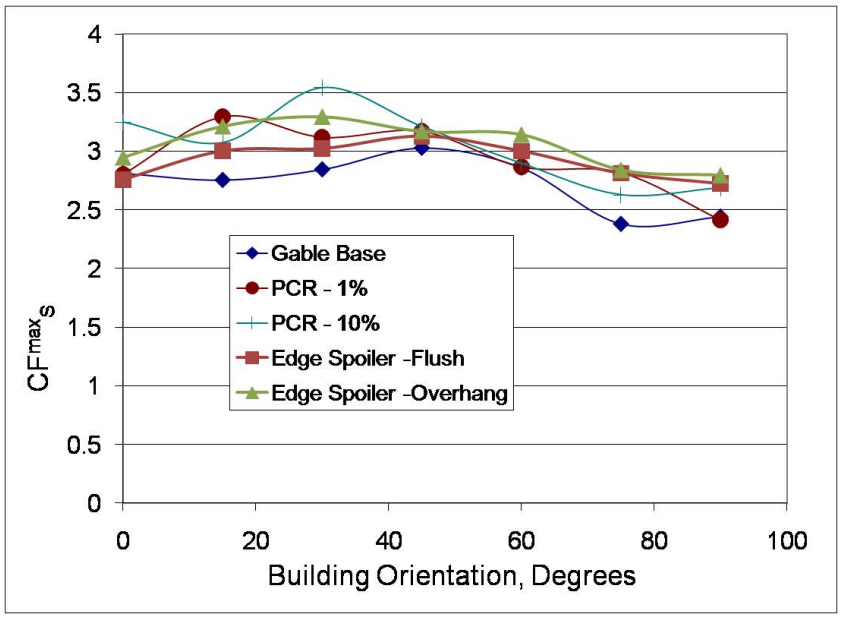

Figure B.5 Peak shear force coefficient plot

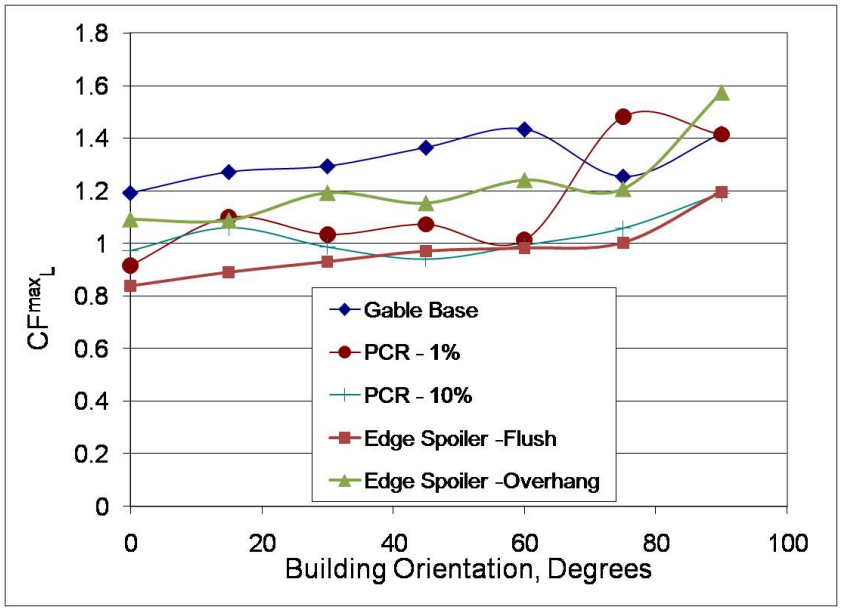

Figure B.6 Peak lift force coefficient plot

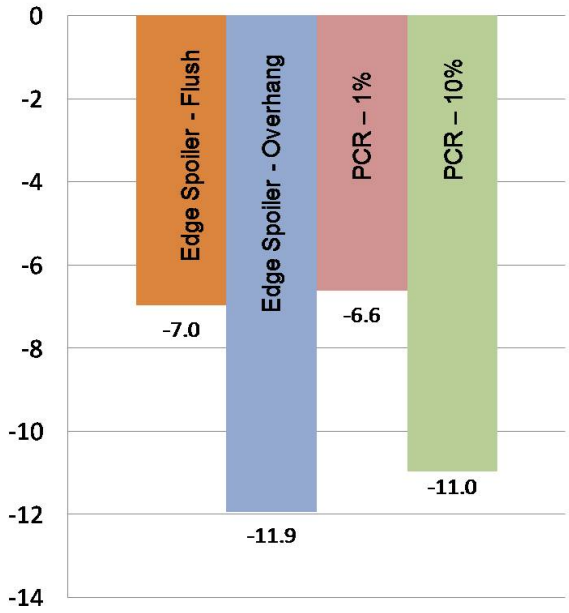

Figure B.7 Percent difference of peak shear force coefficient

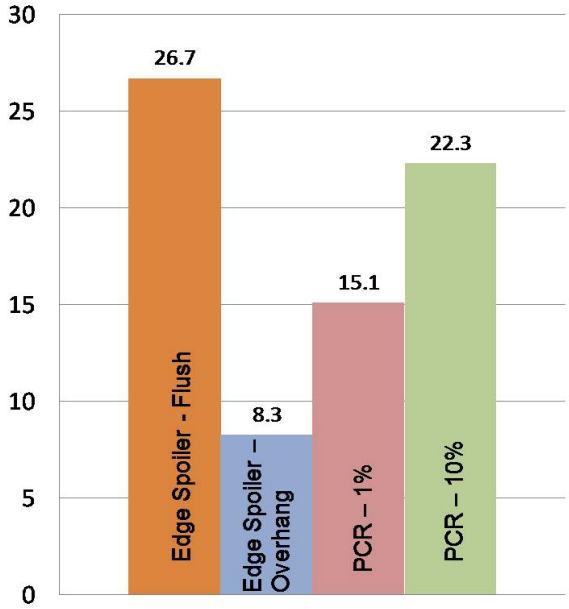

Figure B.8 Percent difference of peak lift force coefficient

APPENDIX C RESULTS OF PASSIVE PRESSURE EQUALIZATION MODELS

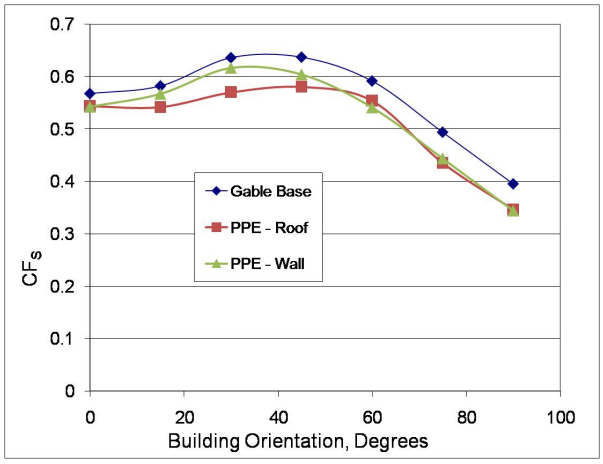

Figure C.1 Mean shear force coefficient plot

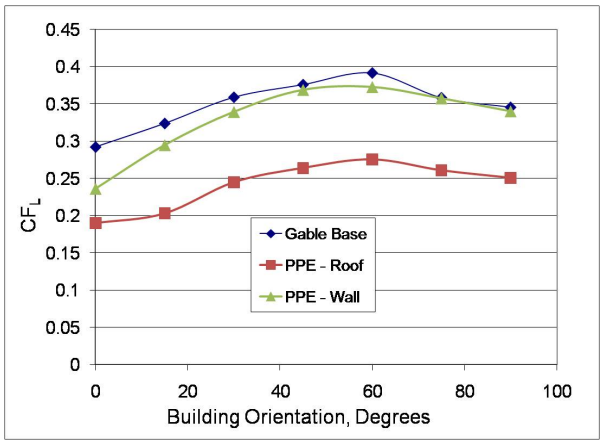

Figure C.2 Mean lift force coefficient plot

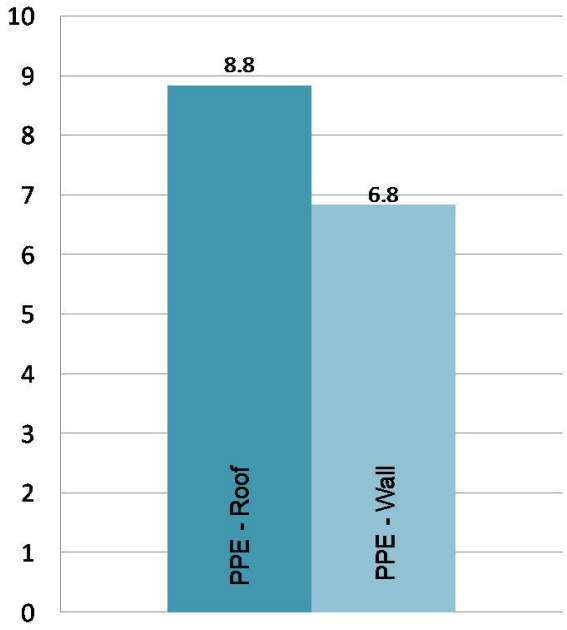

Figure C.3 Percent difference of mean shear force coefficient

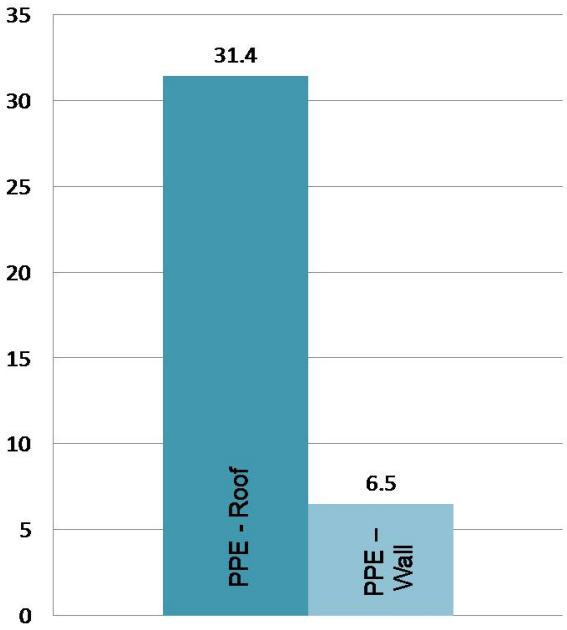

Figure C.4 Percent difference of mean lift force coefficient

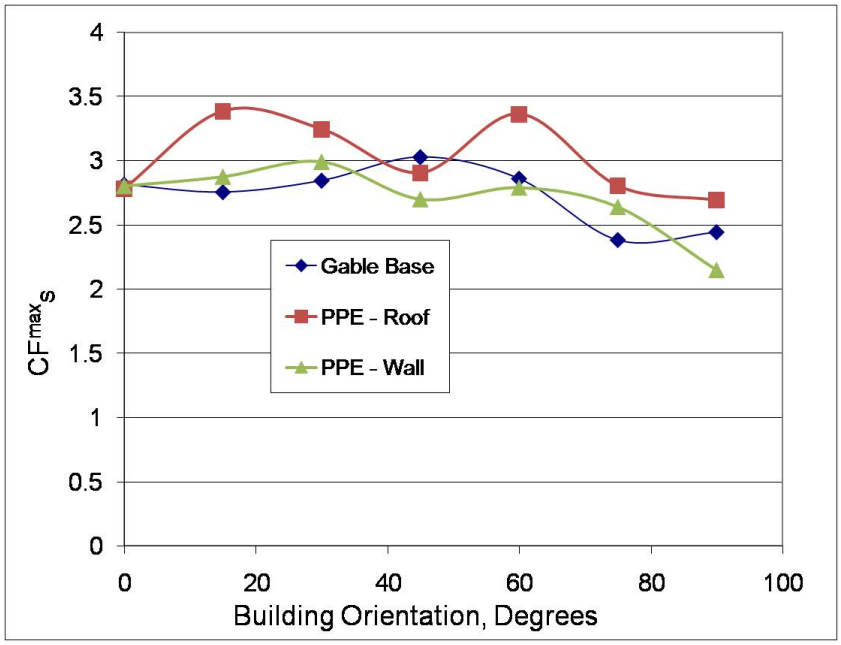

Figure C.5 Peak shear force coefficient plot

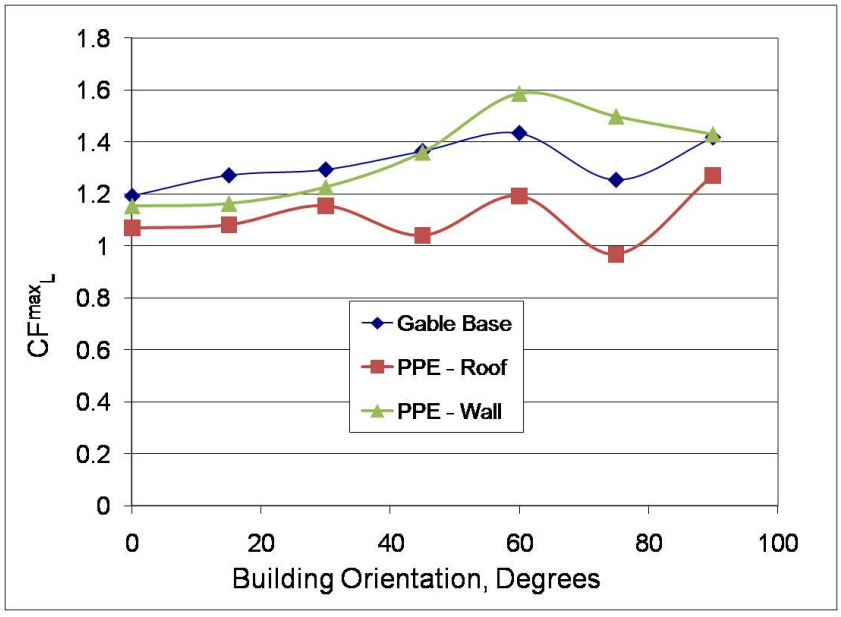

Figure C.6 Peak lift force coefficient plot

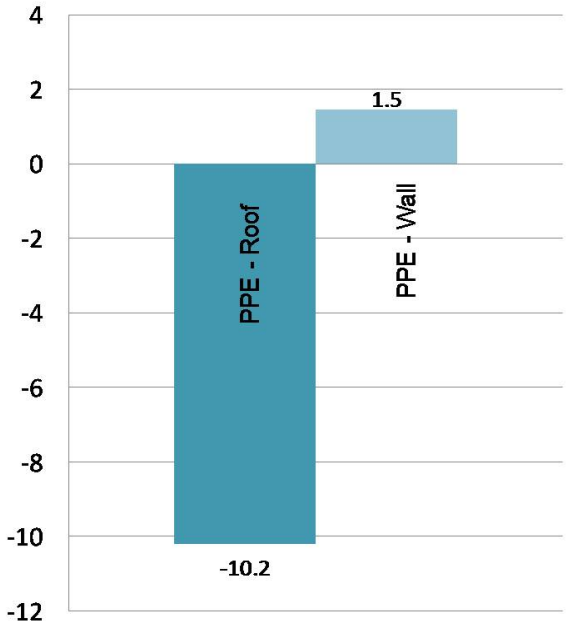

Figure C.7 Percent difference of peak shear force coefficient

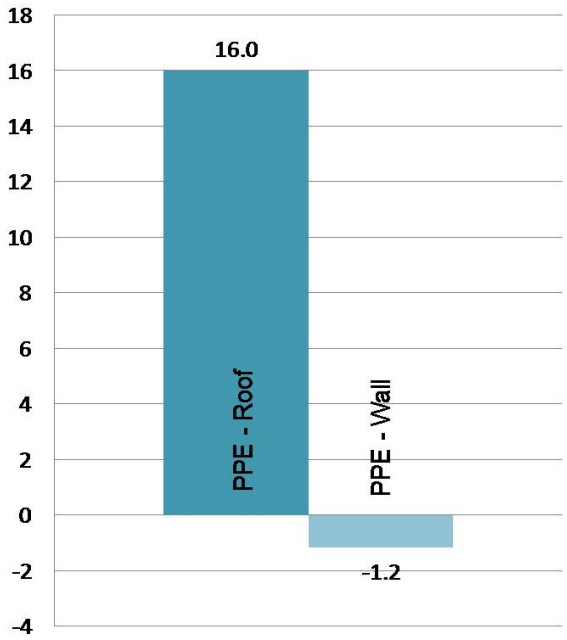

Figure C.8 Percent difference of peak lift force coefficient

APPENDIX D RESULTS OF ALL MITIGATION MODELS

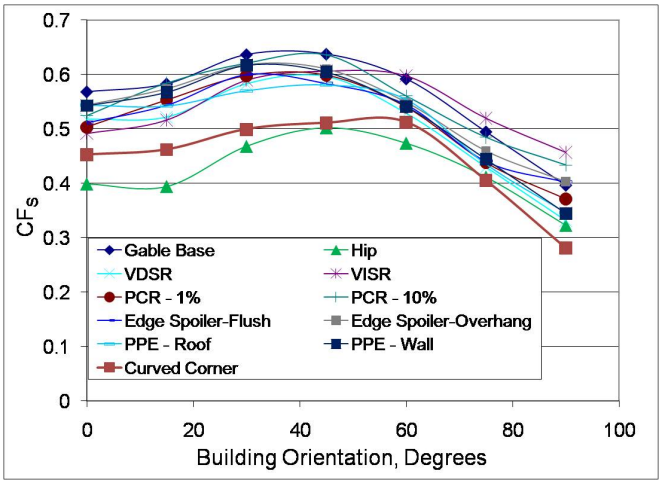

Figure D.1 Mean shear force coefficient plot

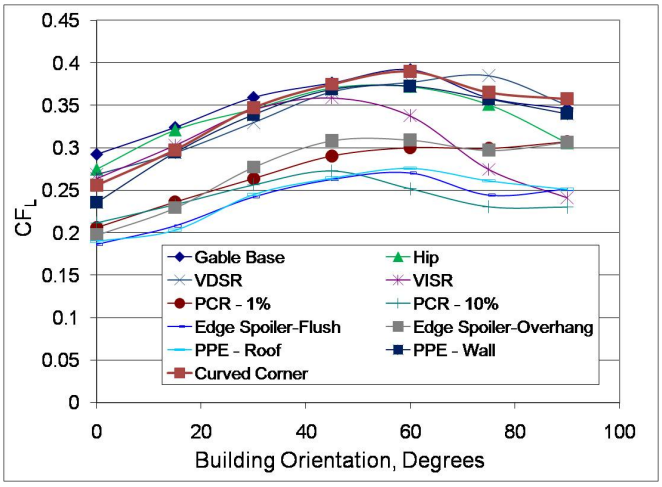

Figure D.2 Mean lift force coefficient plot

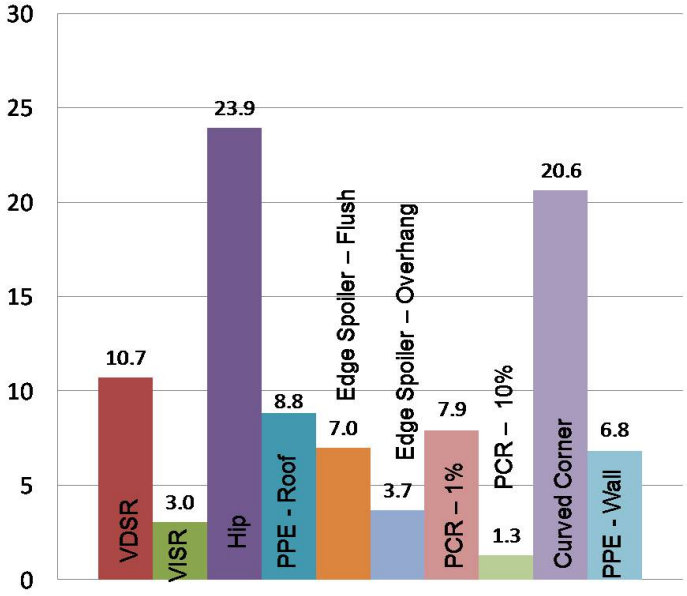

Figure D.3 Percent difference of mean shear force coefficient

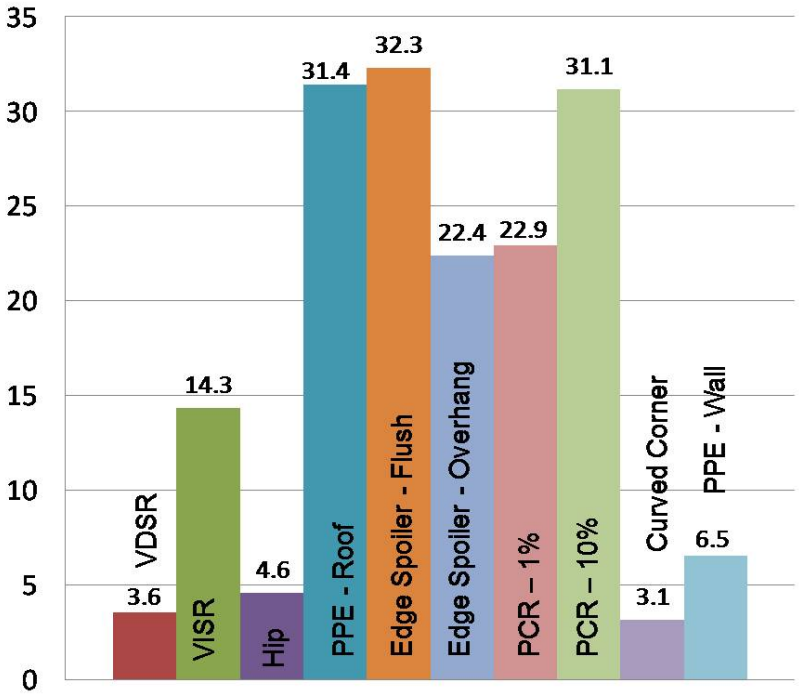

Figure D.4 Percent difference of mean lift force coefficient

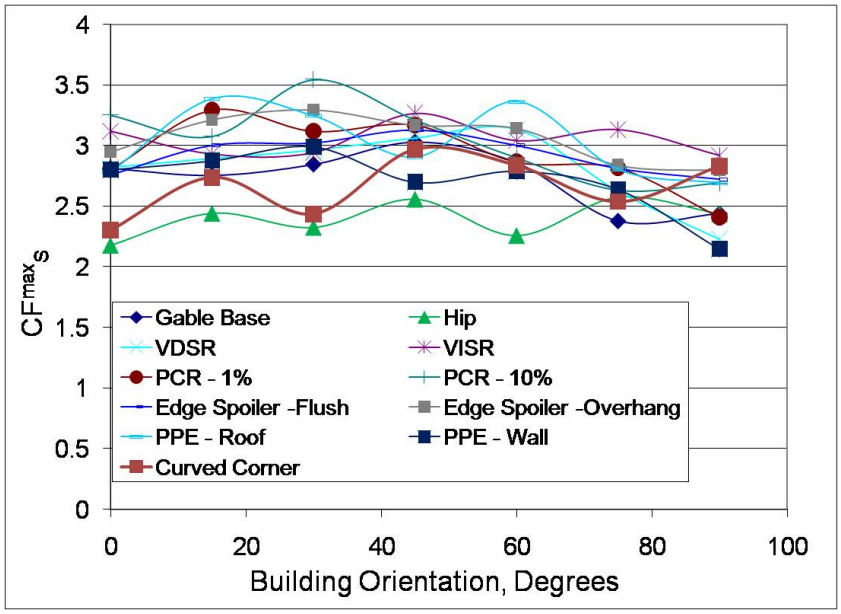

Figure D.5 Peak shear force coefficient plot

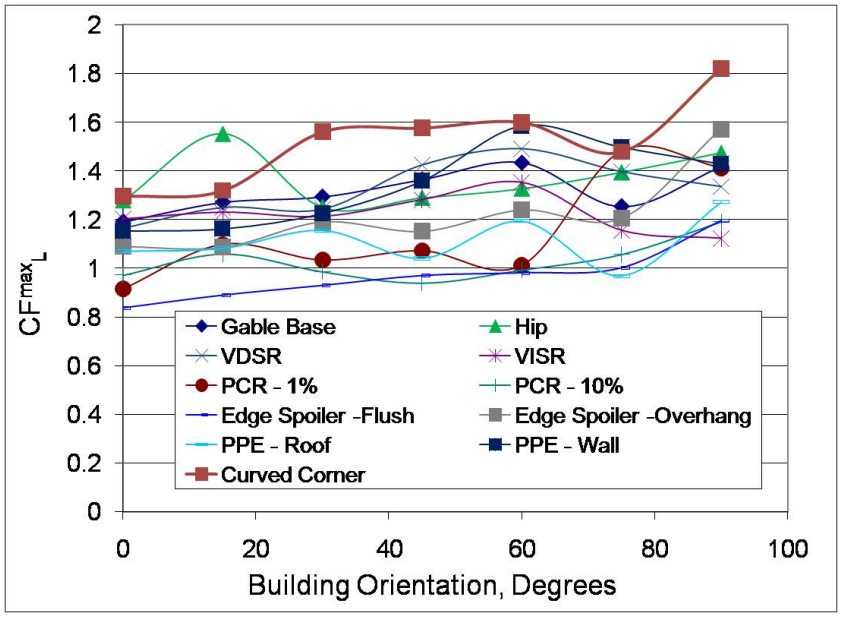

Figure D.6 Peak lift force coefficient plot

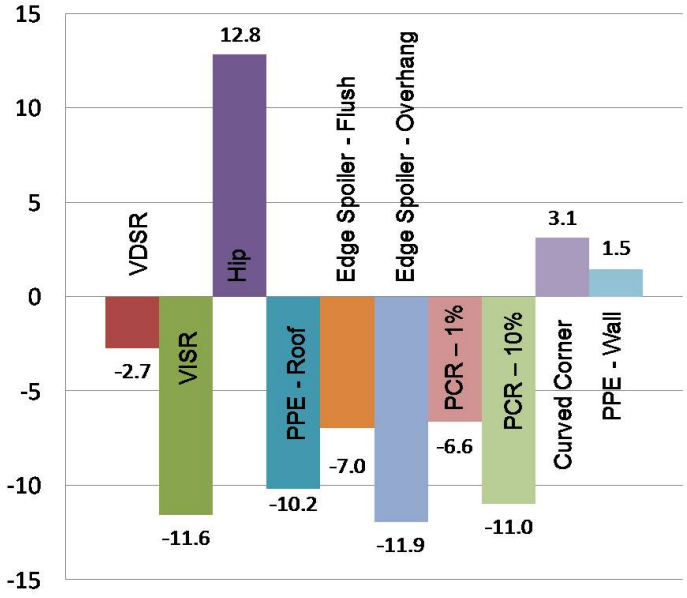

Figure D.7 Percent difference of peak shear force coefficient

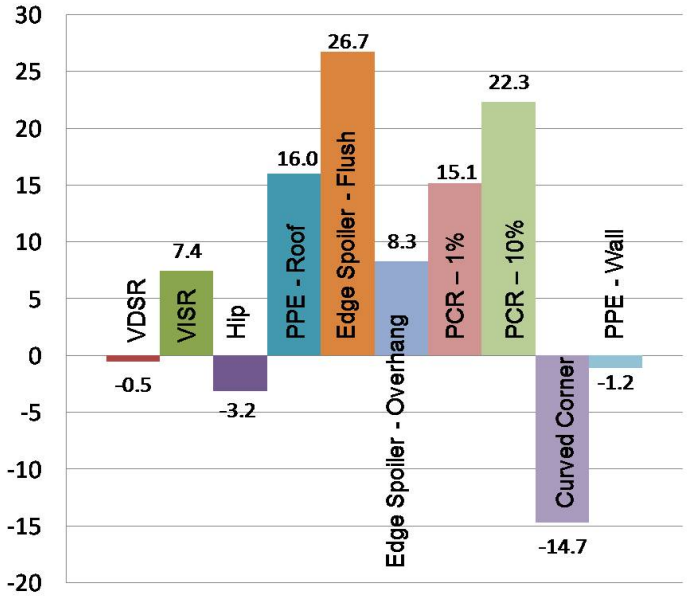

Figure D.8 Percent difference of peak lift force coefficient

BIBLIOGRAPHY

[1] Balaramudu, V., (2007). *Tornado-induced wind loads on a low-rise building*, Master's thesis, Iowa State University, Ames, IA.

[2] Bolton, D., (1980). "The computation of equivalent potential temperature" *Monthly Weather Review* vol. 108: 1046-1053

[3] Case, P.C., Isyumov, N.,(1998). "Wind Loads on low buildings with 4:12 gable roofs in open country and suburvan exposures." *Journal of Wind Engineering and Industrial Aerodynamics* Vol. 77 & 78: 107-118

[4] Cheung, J.C.K., Melbourne, W.H.,(1988). "Wind loading on a porous roof." *Journal of Wind Engineering and Industrial Aerodynamics* Vol. 29: 19-28

[5] Cope, A.D., Gurley, K.R., Gioffre, M., Reinhold, T.A., D.,(2005). "Low-rise gable roof wind loads: Characterization and stochastic simulation." *Journal of Wind Engineering and Industrial Aerodynamics* Vol. 93: 719-738

[6] Franchini, S., Pindado, S., Meseguer, J., San-Andres, A.,(2005). "A parametric, experimental analysis of conical vortices on curved roofs of low-rise buildings" *Journal of Wind Engineering and Industrial Aerodynamics* Vol. 93: 639-650

[7] Hurricane Statistics, City of Texas City-An All-American City, (2007). *http://www.texas-city-tx.org/HurricanesStat.html*

[8] Hurrican Facts, Lundy Wilder, (2008). *http://www.Gulf-Shore-Alabama.net*

[9] Hurrican structure, *http://hurricanewaves.org/images/structure.jpg*

[10] Jones, E., (2008). *Experimental simylation of atmospheric boundary layers and extreme gust events*, Master's thesis, Iowa State University, Ames, IA.

[11] Kuethe, A. M., Chow, C. Y., (1998) *Foundations of Aerodynamics* New Jersey: John Wiley & sons, Inc., p 357-364

[12] Kopp, G., Mans, C., Surry, D.,(2005). "Wind effects of parapets on low buildings: Part 4. Mitigation of corner loads with alternative geometries." *Journal of Wind Engineering and Industrial Aerodynamics* Vol. 93: 873-888

[13] Kubo, Y., Yukoku, E., Modi, V.J., Yamaguchi, E., Kato, K., Kawamura, S.,(1999). "Control of flow separation from leading edge of a shallow rectangular cylinder through momentum injection." *Journal of Wind Engineering and Industrial Aerodynamics* Vol. 83: 503-514

[14] Munshi, S.R., Modi, V.J., Yokomizo, T.,(1997). "Aerodynamics and dynamics of rectangular prisms with momentum injection." *Journal of Fluids and Structures* Vol. 11: 873-892

[15] Meecham, D.,(1992). "The improved performance of hip roofs in extreme winds - A case study." *Journal of Wind Engineering and Industrial Aerodynamics* Vol. 41-44: 1717-1726

[16] Modi, V.J., Fernando, M.S.U.K., Yokomizo, T.,(1991). "Moving surface boundary-layer control as applied to two-dimensional and three-dimensional bluff bodies." *Journal of Wind Engineering and Industrial Aerodynamics* Vol. 38: 83-92

[17] Pielke, R. Jr., Pielke, R. Sr.,(1997). *Hurricanes: Their Nature and Impact on Society*, England: John Wiley & Sons Ltd., p 68-79.

[18] Pindado, S., Meseguer, J.,(2003). "Wind tunnel study on the influence of different parapets on the roof pressure distribution of low-rise buildings." *Journal of Wind Engineering and Industrial Aerodynamcis* Vol. 91: 1133-1139

[19] Wikipedia, (2008). *http://en.wikipedia.org/wiki/Saffir-Simpson_Hurricane_Scale*

[20] Yih, C. S.,(1969). *Fluid Mechanics: A Concise Introduction to the Theory* McGraw-Hill Inc.,p 300-305, 360-362

[21] Wu, F.,(2000). *Full-scale study of conical vortices and their effects near roof corners*, Ph.D. Dissertation, Texas Tech University, Lubbock, Texas.